Engineering Geology 252 (2019) 145–163

Contents lists available at ScienceDirect

Engineering Geology

journal homepage: www.elsevier.com/locate/enggeo

Detection and geometric characterization of rock mass discontinuities using a 3D high-resolution digital outcrop model generated from RPAS imagery – Ormea rock slope, Italy

Niccolò Menegoni[a], Daniele Giordan[b,*], Cesare Perotti[a], Dwayne D. Tannant[c]

[a] University of Pavia, Pavia, Italy
[b] National Research Council of Italy, Research Institute for Geo-Hydrological Protection (CNR-IRPI), Torino, Italy
[c] University of British Columbia, Kelowna, Canada

ARTICLE INFO

Keywords:
Remotely piloted aerial ystems
Rock slope instabilities
Textured digital outcrop models
Discontinuity mapping
Semi-automatic discontinuity identification

ABSTRACT

The use of a remotely piloted aircraft system (RPAS) and digital photogrammetry is valuable for the detection of discontinuities in areas where field mapping and terrestrial photogrammetry or laser scanner surveys cannot be employed because the slope is unsafe, inaccessible, or characterized by a complex geometry with areas not visible from the ground. Using the Structure-from-Motion method, the acquired images can be used to create a 3D texturized digital outcrop model (TDOM) and a detailed point cloud representing the rock outcrop. Discontinuity orientations in a complex rock outcrop in Italy were mapped in the field using a geological compass and by manual and automated techniques using a TDOM and point cloud generated from RPAS imagery. There was a good agreement between the field measurements and manual mapping in the TDOM. Semi-automated discontinuity mapping using the point cloud was performed using the DSE, qFacet FM, and qFacet KD-tree methods applied to the same 3D model. Significant discrepancies were found between the semi-automatic and manual methods. In particular, the automatic methods did not adequately detect discontinuities that are perpendicular to the slope face (bedding planes in the case study). These differences in detection of discontinuities can adversely influence the kinematic analysis of potential rock slope failure mechanisms. We use the case study to demonstrate a workflow that can accurately map discontinuities with results comparable to field measurements. The combined use of TDOM and RPAS dramatically increases the discontinuity data because RPAS can supply a good coverage of inaccessible or hidden portions of the slope and TDOM is a powerful representation of the reality that can be used to map discontinuity orientations including those that are oriented perpendicular to the slope.

1. Introduction

Detection and mapping of rock discontinuities are important not only for geological studies (e.g. structural geology and rock mechanics) but also for engineering and industrial applications (e.g., slope stability, tunneling, quarry activity, CO_2 and nuclear waste storage, oil and gas exploitation). Therefore, the acquisition of accurate quantitative discontinuity data, which are not affected by biases and censoring is very important. A recent tool that can be useful for this purpose is a Digital Outcrop Model (DOM) (Powers et al., 1996).

In the past twenty years, the applications in geosciences of remote sensing investigations for the construction of DOM have rapidly improved (e.g. Powers et al., 1996; Xu et al., 2000; Pringle et al., 2004; Bellian et al., 2005; Sturzenegger and Stead, 2009; Jaboyedoff et al., 2012; Westoby et al., 2012; Humair et al., 2013; Bemis et al., 2014; Spreafico et al., 2016; Tavani et al., 2016). The most common techniques used to generate highly detailed DOMs are terrestrial laser scanning and digital photogrammetry. While laser scanning can be very expensive and requires complex survey planning (heavy and bulky equipment), digital photogrammetry allows for acquisition of high-resolution data with a lower cost and with more user-friendly survey planning (Remondino and El-Hakim, 2006; Westoby et al., 2012). Developments in RGB cameras and Remotely Piloted Aircraft Systems (RPAS) (Colomina and Molina, 2014) have increased the applications of RPAS-based Digital Photogrammetry (RPAS-DP) in geosciences (Niethammer et al., 2012; Westoby et al., 2012; Lucieer et al., 2013; Bemis et al., 2014; Tannant, 2015; Casella et al., 2016; Salvini et al., 2017; Chesley et al., 2017; Giordan et al., 2017; Török et al., 2017).

---

[*] Corresponding author.
E-mail address: daniele.giordan@irpi.cnr.it (D. Giordan).

https://doi.org/10.1016/j.enggeo.2019.02.028
Received 9 March 2018; Received in revised form 22 February 2019; Accepted 26 February 2019

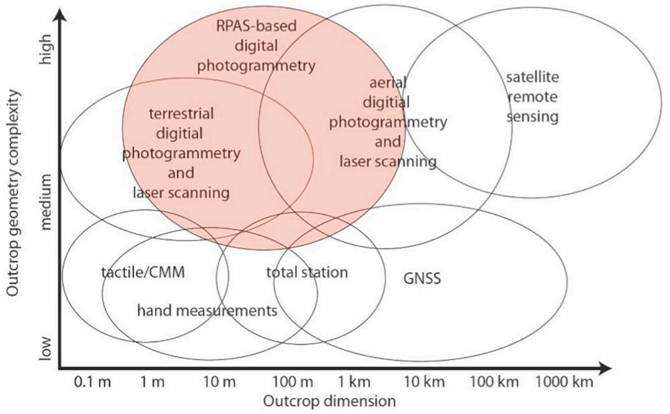

Fig. 1. Applicability of different mapping techniques in relation to the outcrop dimensions and geometry complexity (modified after Nex and Remondino, 2014).

RPAS-DP can be used in a wide variety of scenarios (Nex and Remondino, 2014; Fig. 1), from meter scale (e.g. Cawood et al., 2017; Tannant et al., 2017) to kilometer scale (e.g. Gonçalves and Henriques, 2015) and from simple geometries (e.g. Chesley et al., 2017) to complex geometries (e.g. Cawood et al., 2017). Moreover, RPAS-DP can also overcome the occlusion effects that often affect terrestrial photogrammetry and laser scanning techniques because the RPAS platform can remotely move the camera to more optimum user-inaccessible positions. The use of different points of view is important for the reduction of occlusions or areas that cannot be measured using terrestrial technologies that are restricted to data collection from the ground.

Due to the presence of a GNSS/INS system on an RPAS platform, it is possible to measure the camera location for each image that is taken. This then allows for direct georeferencing of photogrammetric products produced using Structure-from-Motion (SfM) digital processing of the images (Nex and Remondino, 2014).

The principal products from SfM-based image processing are: (i) Point Cloud (PC), (ii) Digital Surface Model (DSM), (iii) orthoimage, and (iv) 3D texturized model. In geoscience, the latter product is also called Texturized Digital Outcrop Model (TDOM). The resolution of these SfM-based photogrammetric products depends directly on the resolution of the camera sensor (number of pixels and pixel size), the camera lens (focal length) and the distance between the camera and the object. The accuracy depends on the quality of the camera and RPAS components (e.g. camera lens, internal and external camera stabilizer, GNSS/IMU system), the RPAS-DP survey planning (e.g. image overlap, weather and lighting conditions, presence or absence of ground control points) and the SfM processing (e.g. camera calibration and orientation).

Giordan et al. (2015) proposed two different kinds of RPAS-DP surveys for landslide applications (Fig. 2): (a) RPAS-DP survey for steep slopes (slope angle > 40°, usually rock slopes) and (b) RPAS-DP survey for moderate to gentle slopes (slope angle < 40°). These two kinds of survey differ by camera view direction. When conducting the survey, an oblique or even horizontal camera view may work best for steep slopes whereas a vertical or nadir camera view is typically best for gentle slopes. A multirotor RPAS is often used for steep slopes while multirotor or fixed-wing RPAS can be used for gentle slopes. This conceptual differentiation of RPAS surveys can be applied not only to landslide studies but also to other geological studies in similar terrain.

In geoscience applications, the DSM and orthoimage can be managed with GIS software and base-level computers. However, the PC and TDOM typically require specific 3D rendering software and a computer with a medium to high-level graphics card. Usually, due to the presence of a large amount of information, a TDOM requires a higher graphics card performance than a PC. For the analysis of discontinuities in a rock outcrop, a PC or TDOM are required because they allow for selection of 3D point positions that belong to a discontinuity thus allow for a fitting of a plane to a set of points representing the discontinuity. Whereas a PC is composed of 3D points, TDOMs are 3D meshes consisting of triangular facets filled with image texture in the space between the points defining the facet vertexes. Therefore, a TDOM can significantly improve the identification and the correct interpretation of discontinuity traces that cannot be detected in a PC.

The detection of discontinuities in a DOM can be done manually or automatically. Recently, several different algorithms for the semi-automatic detection of discontinuities have been proposed, such as DSE (Riquelme et al., 2014) and qFacet (Dewez et al., 2016). Most of these methods work on a PC and use an algorithm of the k-nearest neighbor (knn).

In this study, RPAS-DP was used as a tool to identify and map the discontinuities contained within a sub-vertical rock slope. The rock slope has a complex geometry, and it generates rockfalls. The discontinuity detection was done using both manual and automatic methods, and the results from each method are compared in terms of discontinuity geometry and kinematic instability analysis. The case study demonstrates a workflow for the detection of discontinuities in a sub-vertical rock slope.

2. Study site

The study area is located in the western portion of the Ligurian Alps, near the village of Ormea (CN, Italy) along the Tanaro Valley (44.147° lat., 7.919° long.). On the right side of the river, a vertical rock slope characterized by recurrent instability phenomena imperils roads, a bridge, some houses, and the riverbed that are just below it (Fig. 3).

The rock slope is approximately 100 m wide and 80 m high and is composed principally of quartzites. The studied area is characterized by the presence of several large joints at the base of the slope that can cause the collapse of large sections of the rock bluffs, especially in the central sector. These joints are monitored by ARPA Piemonte (Regional

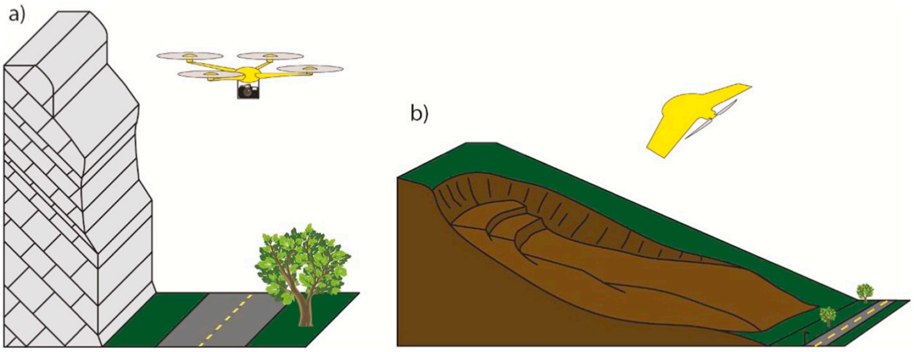

Fig. 2. Different RPAS survey options proposed by Giordan et al. (2015) for (a) steep rock slopes and (b) gentle to moderate slopes.

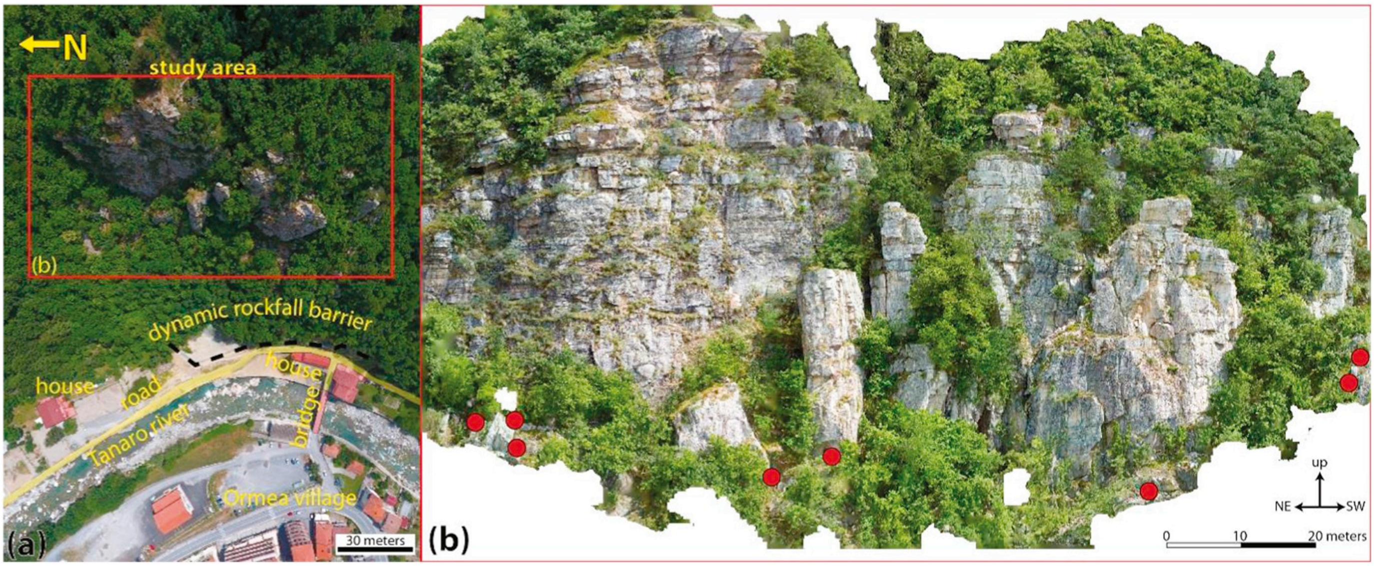

Fig. 3. RPAS-based images: (a) nadir image of the rock slope and the village below and (b) orthorectified image of the rock outcrop. Red dots indicate the position of the control planes measurable in the field and visible and measurable in the images acquired by RPAS. (For interpretation of the references to colour in this figure legend, the reader is referred to the web version of this article.)

Environmental Protection Agency), and some movements were registered after a flood event that occurred in the Piemonte in November 2016. Furthermore, some unstable blocks were detected in the southwestern sector immediately after the flood. For this reason, some blocks were removed, and rockfall nets were installed at the base of the slope.

The field investigations were conducted with a goal to measure the main joint sets and to identify the most unstable areas. Due to the presence of inaccessible unstable sectors of the rock wall, an innovative solution that considered the use of remote sensing techniques was evaluated for a better characterization of these areas. The complex geomorphology, topography, and the existence of trees at the site, immediately highlighted the main limitations of terrestrial photogrammetry and laser scanning. These methods were only able to acquire data for limited portions of the slope. In addition, the presence of potentially unstable blocks limited safe access to the entire slope for a manual acquisition of discontinuity data. For this reason, the use of RPAS was considered a good solution for the acquisition of a nadir and oblique dataset (Fig. 3).

2.1. Geology

In the Ormea area, the different geological units that compose the central Ligurian Alps (External and Internal Briançonnais, Pre-Piedmont and Piedmont Ligurian units) are stacked upon each other (Fig. 4). The slope that was examined is formed by a succession of rock belonging to the lower part of the External Briançonnais. These lie over a Pre-Namurian metamorphic basement and the clastic Permian succession of the Ollano Formation, which are not exposed in the area. The following lithological units are present:

- Melogno Porphiroids (Early Permian) – calc-alkaline rhyolitic and rhyodacitic volcanic ignimbrites and pyroclastics.
- Verrucano Formation (Late Permian) – well-rounded polygenic conglomeratic continental deposits, strongly cemented, with interbedded green and violet schists and whitish conglomerates and sandstones. The formation rests paracomformably on the eroded top of the volcanic complex of the Melogno Porphiroids.
- Ponte di Nava Quartzites (Early Triassic) – coarse-grained grey quartz arenites and conglomerates with fining-upwards cycles. The lower part of the formation is characterized by a coarser facies with rough bedding, while the upper part is composed of thinner beds of medium-to-fine quartz arenites interbedded with greenish pelites.
- San Pietro dei Monti Dolomite (Ladinian) – massive to well-bedded grey dolostones and limestones forming a thick carbonate platform succession (about 200 m).

Along the right slope of the Tanaro valley, the described succession is tectonically truncated at the level of the San Pietro dei Monti Dolomite by the large sub-horizontal fault that thrusts the Inner Units (Internal Briançonnais, Pre-Piedmont, and Piedmont Ligurian units) over the External Briançonnais.

The rock cliff in the study area contains sub-horizontal bedding and large sub-vertical discontinuities that delineate rocky pinnacles characterized by rockfalls and instability phenomena. To the north of the cliff, some NE to ENE tectonic lineaments were detected by the analysis of two sets of aerial photographs and partially verified by field surveys (Fig. 4). One of them coincides with a fault that borders the Melogno Porphiroids.

3. Methodology

A RPAS was used to acquire a series of high-resolution images of the inaccessible rock cliff that is characterized by a complex geometry with several areas that cannot be seen from the ground level. The images were then converted into a TDOM using Structure-from-Motion (SfM) software.

A classic field survey with a geological compass-clinometer was performed to measure 145 discontinuities at the bottom of the slope, where the field conditions allowed for safe manual acquisition of direct measurements. Differences between the compass-based field measurements of the orientations of the control planes and discontinuities and the orientations extracted from the TDOM were evaluated. We also measured the orientation of 8 control planes found near the toe of the rock slope. These planes were also visible in images acquired by RPAS. This dataset was used to evaluate the accuracy of the discontinuities identified in the TDOM and was used to validate the TDOM orientation generated without the use of GCPs.

Discontinuity analysis using the TDOM was done with semi-automatic and manual mapping methods. In this paper, we present the results from both approaches, and we propose a composite method for discontinuity identification that involves manual validation of preliminary automatic mapping results. In particular, the manual mapping

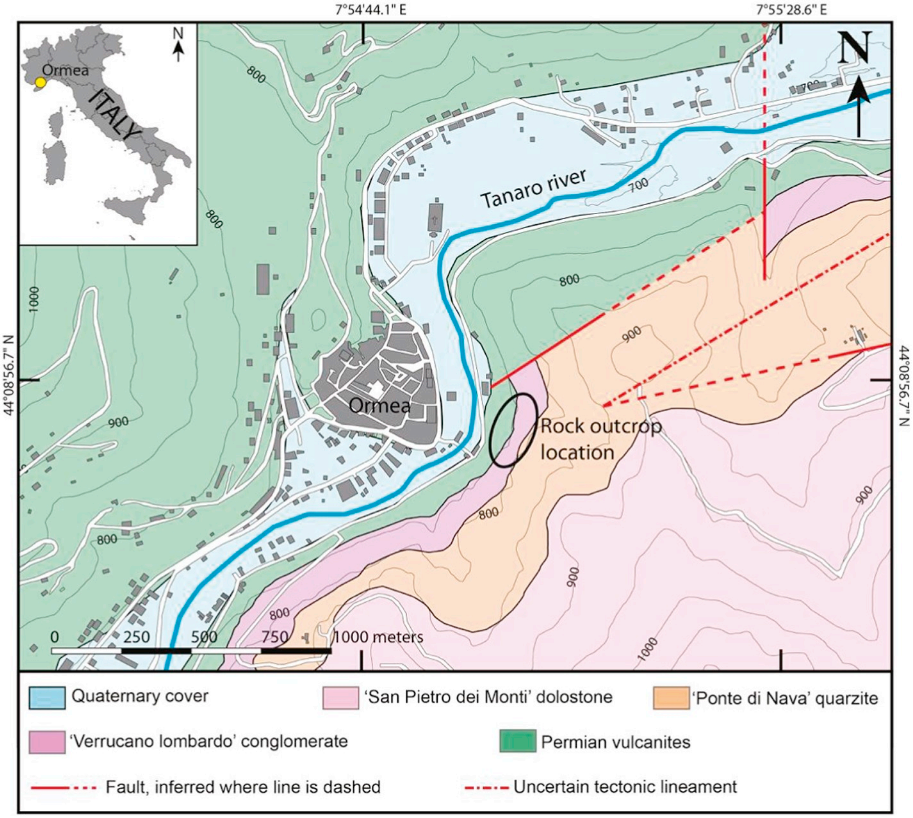

Fig. 4. Geological map of the study area.

using the highly detailed TDOM allows for the recognition of discontinuities that are orthogonal to the rock wall and that are often identifiable only as traces without 3D relief and no visible plane surfaces (Seers and Hodgetts, 2016; Biber et al., 2018). For this reason, the semi-automatic methods based on the coplanarity test of the points of the PC can often underestimate these geological structures.

The main steps of the proposed methodology are schematically indicated in Fig. 5.

3.1. RPAS digital photogrammetric survey and image processing

The RPAS-based digital photogrammetric survey was conducted with an oblique orientation for the on-board camera, and 236 digital photographs were acquired. The collected images had a minimum overlap and sidelap of about 90% and 80%, respectively. In order to capture the complex geometry of the outcrop and to improve the precision of the generated TDOM, the images were acquired from positions parallel (strips of photographs taken along a fly line) and convergent to the outcrop (Birch, 2006). The average distance from the camera to the closest rock surface was 32 m, with a standard deviation of 11 m (Fig. 6). The flights were flown under manual control in a sequence of back-and-forward flight lines to cover the full vertical extent of the rock outcrop.

The features of the RPAS platform and on-board camera are reported in Table 1.

The RPAS was equipped with a GNSS/IMU, and all the acquired images were georeferenced in a WGS84/UTM32N metric coordinate system. Moreover, to obtain a high accuracy model 22 points on the slope were measured with a Topcon GPT-7001L total station (15 were used as Ground Control Points – GCPs – and 7 as Check Points – CKPs). The GCPs and CKPs positions are shown in Fig. 7. The GCPs network was georeferenced using four different points acquired by the robotized total station and a Leica 1200 GPS RTK.

The TDOMs or 3D digital models were created with the Structure-from-Motion (SfM) technique using Photoscan Professional v.1.2.5 software (Agisoft, 2016), which is widely employed in earth sciences studies (e.g. Turner et al., 2014; Gonçalves and Henriques, 2015; Casella et al., 2016; Cawood et al., 2017; Jordá Bordehore et al., 2017; Salvini et al., 2017). Due to the presence of the 22 GCPs acquired using a total station, we decided to develop two different 3D models. The procedures used during the processing were the same for the two models, except for the use of GCPs for the georeferenced model versus direct-georeferencing using only the RPAS on-board GPS. For a detailed description of the technique, see Lucieer et al. (2013) and Turner et al. (2014). The processing steps are summarized below.

3.1.1. Image pre-processing

All 236 images were georeferenced using the coordinates registered by the on-board GPS; 12 images with blur effects were discarded.

3.1.2. Image matching, bundle block adjustment, and creation of sparse PC

224 images were aligned using the highest accuracy (full resolution matching) and using the pair pre-selection method that takes into account the image positions registered by the RPAS-GPS. Then the bundle block adjustment was computed using the positions of the 15 GCPs measured using the total station. The accuracy of the GCPs was imposed as 50 mm. A sparse PC of 505,081 points was obtained.

3.1.3. Dense PC creation

Using the high-resolution images (38 Mpx), a dense PC was developed using the *high* quality parameters of the Photoscan procedure (i.e. all the images were subsample at a factor 2 in each dimension), and a *mild* depth filtering. A dense PC of ~98 million of points was generated at the end of the process. The mean surface density of the PC was around 1000 points per m^2.

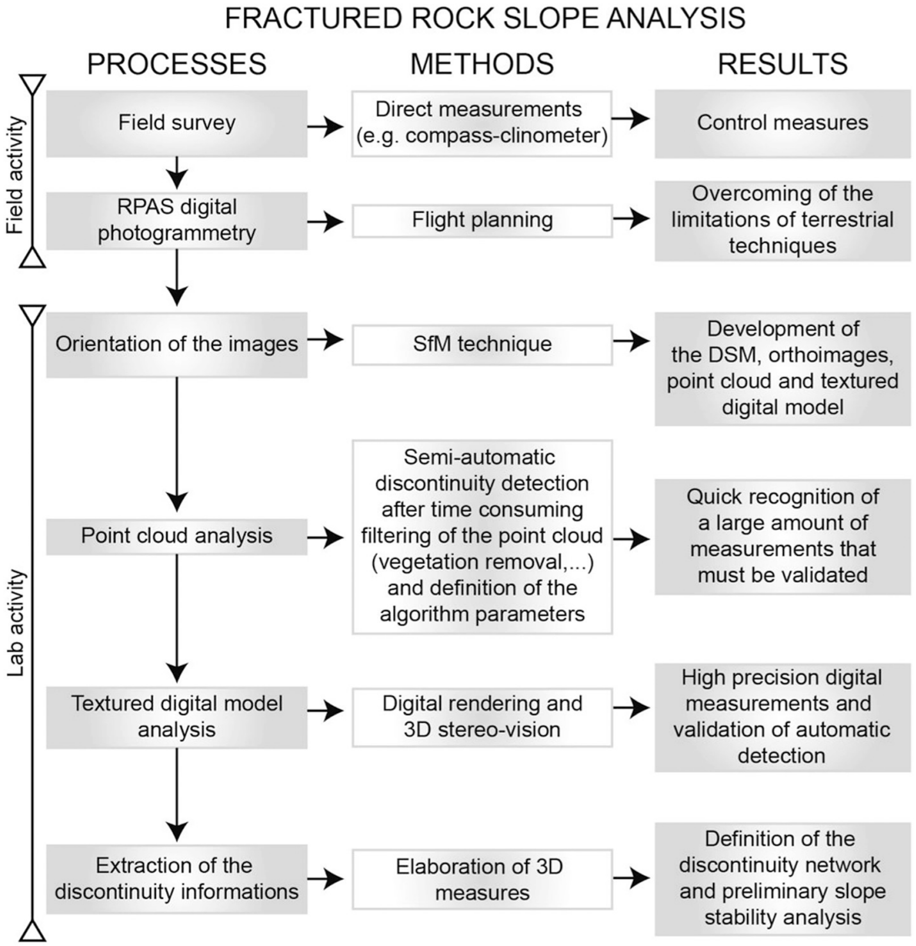

Fig. 5. Conceptual scheme of the proposed workflow.

3.1.4. Mesh creation

After a manual removal of the highly vegetated areas, a 3D mesh was constructed selecting the *high* face count suggested by the software. A mesh with ~35 million faces for a total surface of 12,744 m^2 was developed at the end of the process.

3.1.5. Texture mapping and orthophoto mosaic generation

A *generic* texture mapping and a *mosaic* blending mode were used to obtain the texture for the mesh, considering only the images with a quality value > 0.7 and developing a texture atlas composed of 10 files with 8 Mpx. Finally, an orthophoto mosaic (Fig. 3b) with a resolution of 6.45 mm/pixel was generated as a TIFF file.

3.1.6. Export of PC and TDOM

The PC and TDOM were exported using a WGS84 metric coordinate system. In particular, the dense PC was exported as a xyz.txt file including the RGB colour value for each point. The TDOM was exported as an OBJ file including the vertex normal and texture.

3.2. Accuracy

The absolute accuracy of the two DOMs (one directly georeferenced using the on-board GPS coordinates and the other by means of 22 GCPs and check points widely distributed across the target area) were calculated by comparing GCPs and check point coordinates measured by the total station and with coordinates of the same points in the models (Table 2).

The comparison shows a satisfying absolute accuracy of the GCP-model, while the model that is directly georeferenced using the on-board GPS coordinates for each photograph is affected by a significant shift, especially in altitude. A shift or translation of the model coordinates is commonly observed when using just the coordinates from the RPAS GPS as these tend to be incorporate an off-set from the actual coordinates. While the RPAS GPS coordinates may be shifted from the actual coordinates, the relative positioning of the coordinates is typically far more accurate. The relative accuracy of the directly georeferenced model was evaluated by comparing the lengths and attitudes of vectors joining pairs of points in the model with the corresponding lengths and attitudes from the GCP-georeferenced model. The maximum angular differences in attitude (Table 3) and length of 20 measured vectors are ± 1° and 0.3%, respectively. Similarly, a comparison of 11 plane attitudes on both models (Table 3) shows a maximum angular difference of ~1°.

Moreover, to validate the results of the RPAS survey, the control planes manually identified using the TDOM were compared with those measured in the field with a geological compass. During the field survey, only a small number of control planes were measured at the toe of the slope because the rest of the outcrop was largely inaccessible and unsafe to work on. The field-measured control planes were chosen because they were clearly visible from the RPAS survey.

The mean dihedral angle (the acute angle determined by the normal vectors of the planes) between the orientations of the control planes determined directly in the field and those measured manually from the TDOM was 3°, with a maximum of about 6° (Table 4). This value suggests that both methods gave similar results given that the typical precision obtained for field collection of discontinuity orientations by a compass is typically between 2° and 5°. Moreover, manual sampling can be affected by an orientation bias due to the local variation of surface

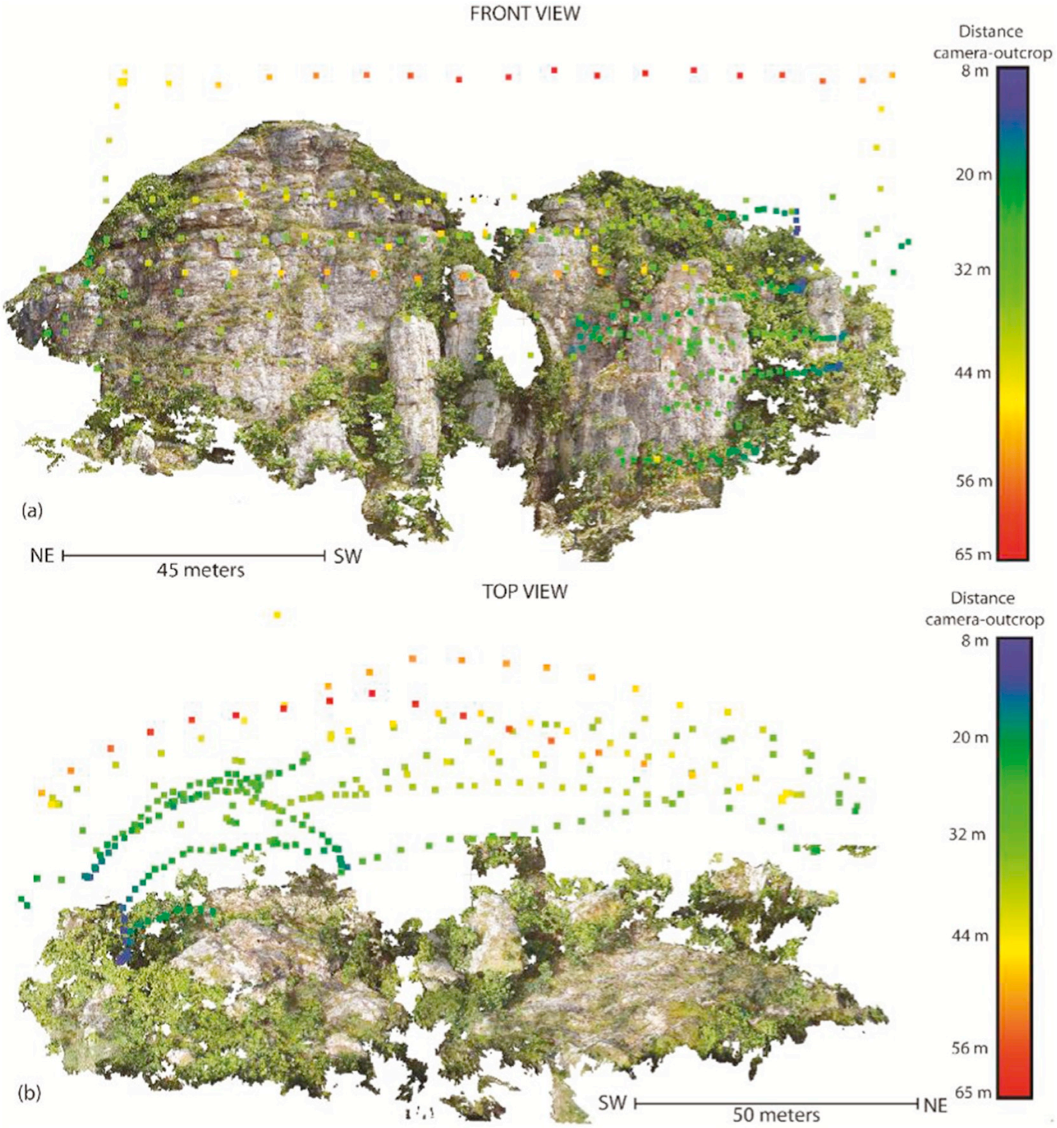

Fig. 6. Front and top view of the rock outcrop showing the camera locations. Point colors indicate the camera-outcrop distance.

orientations, whereas DOM sampling often overcomes this problem because the best-fit plane covers a larger surface area of the discontinuity.

These results confirm the validity of the DOMs. For geological outcrop studies, having a model that is at the correct scale and orientation is certainly more important than having it precisely georeferenced because the measurements (e.g., attitudes of plane and surfaces) calculated in a DOM characterized by good relative accuracy are equivalent to measurements made on the outcrop.

3.3. Discontinuity analysis

Automatic and semi-automatic procedures to identify and map discontinuities have been developed and used by several authors (Slob

Table 1
RPAS and on-board camera specifications.

RPAS system specifications					
RPAS type	Dimension	Engines	Rotor diameter	Empty weight	Payload
V-shaped quadcopter	56 × 80 × 17 cm	4 brushless	381 mm	6.9 kg	8.3 kg

On-board camera specifications					
Camera	Sensor type	Sensor size	Image size	Pixel size	Focal length
SenseFly Albris	CCD	10 × 7.5 mm	7152 × 5368 px	1.4 × 1.4 μm	8 mm

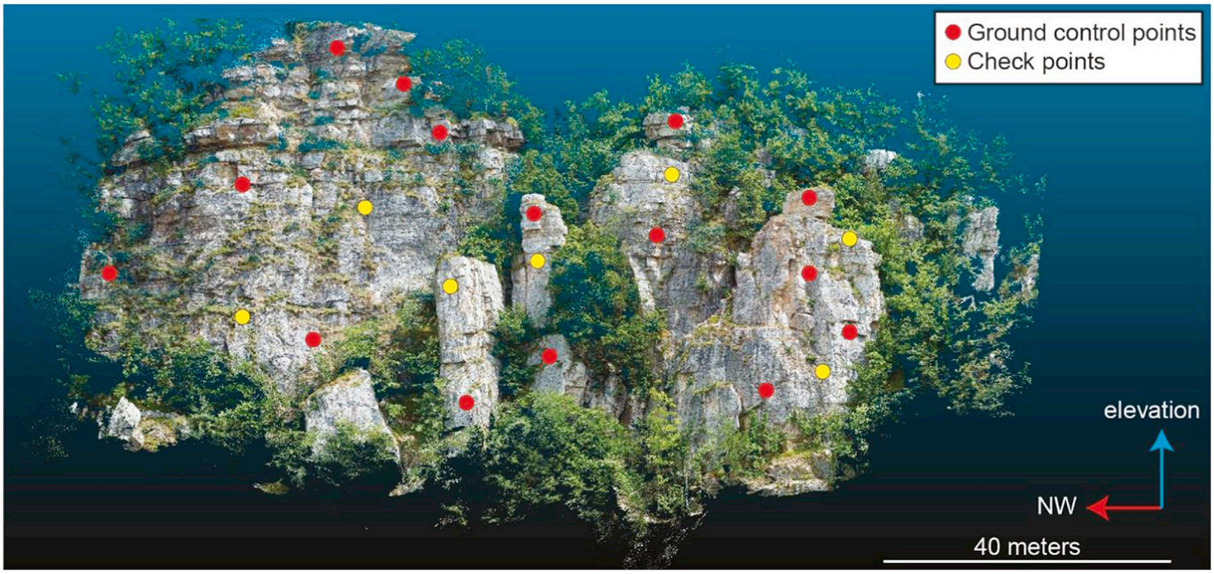

Fig. 7. 3D Point cloud of the rock slope. Red and yellow dots indicate the position of GCPs and CKPs, respectively. (For interpretation of the references to color in this figure legend, the reader is referred to the web version of this article.)

Table 2
Absolute accuracies of GCP and directly georeferenced models evaluated on 15 GCPs and 7 CKPs.

	DOM GCP-georeferenced				DOM directly georeferenced	
	GCP errors (m)		CKP errors (m)		GCP and CKP errors (m)	
	Horizontal	Vertical	Horizontal	Vertical	Horizontal	Vertical
Mean	0.023	0.015	0.033	0.009	0.807	9.401
St. Dev.	0.012	0.012	0.023	0.005	0.136	0.208
Min	0.005	0.001	0.008	0.004	0.611	9.005
Max	0.039	0.049	0.082	0.019	1.097	9.719

Table 3
Relative accuracies of TDOMs evaluated by angular differences in attitude of 20 measured vectors and 11 plane attitudes.

	Lines errors			Planes errors		
	Trend	Plunge	Angle	Dip	Dip Azimuth	Dihedral angle
N° of measures	10	10	10	11	11	11
Mean	1.0	1.2	1.6	0.8	0.5	1.0
St. Dev.	0.4	1.2	1.6	0.4	0.2	0.4
Min.	0.3	0.1	0.2	0.3	0.2	0.4
Max.	1.7	3.3	5.7	1.5	1.0	1.8

Table 4
Comparison between the dip direction/dip (°) of the control planes measured directly on the outcrop (average measurement for a single control plane) and those acquired by manual detection on TDOM.

Plane	Compass	No. measurements	TDOM	Dihedral angle between planes (°)
a	039/69	10	043/75	6.1
b	040/72	8	043/73	1.3
c	040/70	11	043/70	1
d	039/78	13	44/79	5
e	227/80	8	228/85	5.1
f	180/82	6	180/78	4
g	041/86	15	043/87	1
h	226/87	6	221/88	1

et al., 2004; Jaboyedoff et al., 2007; Vöge et al., 2013; Gigli and Casagli, 2011; Chen et al., 2016; Dewez et al., 2016; Gomes et al., 2016; Jordá Bordehore et al., 2017; Guo et al., 2017) and represent important improvements in the use of digital terrain models and/or point-clouds. In this paper, we present the results obtained by manual and semi-automatic procedures, and we show the impact that these two approaches can have on the identification of discontinuity sets and potential instabilities.

3.3.1. Manual detection and mapping of discontinuities

The manual recognition and measurement of the discontinuities were conducted by visualizing and analyzing the TDOM in a stereoscopic environment using a Planar Stereoscopic Mirror SD2220W device. This device has two separate display monitors placed one above the other in a clamshell configuration with a half-silvered glass plate bisecting the angle between the two displays. It is important to emphasize that the identification of the discontinuities was realized by the stereoscopic inspection of the images texturized on the 3D model and not only by examining the point cloud. In fact, the stereo-vision of the texturized model (i.e. examining the real photographic images of the outcrop) allows for a better understanding of the real nature and geometry of the structures to be analyzed (strata, discontinuities, traces of fractures, lineations) and avoids misinterpretation due to 2D visualization on standard monitors of 3D objects depicted by a point cloud.

The measurement of planes that represent discontinuities was performed using the tools in the open-source software CloudCompare v.2.9. After the visual identification of a discontinuity, the points in the cloud belonging to the discontinuity were digitized, and the 3D discontinuity plane to these points was determined using a least-squares best-fit approach. Several measurements were collected for each discontinuity plane or trace, and the average measurement was taken to represent the discontinuity geometry.

The discontinuities were sampled for their entire visible exposure as planes and/or traces to calculate not only their orientation (dip and dip direction) and position, but also their dimensions (discontinuity length).

To evaluate the robustness of the manual detection results obtained using the free software CloudCompare, we repeated the manual mapping of discontinuities using different commercial software. Another operator used 3DM Analyst© photogrammetric software (ADAM Technology) to identify the discontinuities in the same studied area.

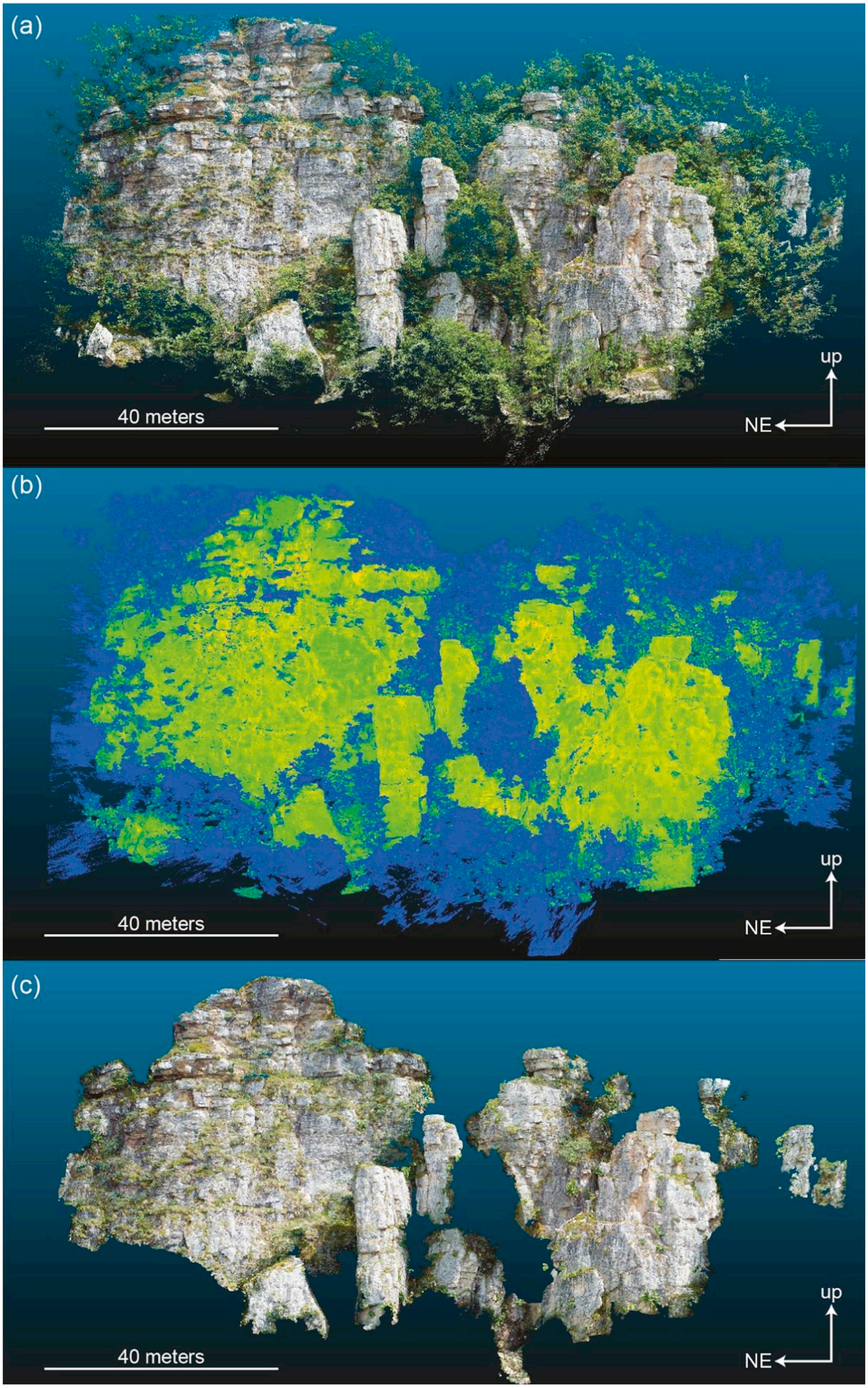

Fig. 8. Vegetation removal process: (a) initial point cloud, (b) classification of points for removal (blue areas) based on RGB and HSV attributes of the points and the low density of the PC in vegetated areas, (c) final PC obtained after the use of the filters. (For interpretation of the references to colour in this figure legend, the reader is referred to the web version of this article.)

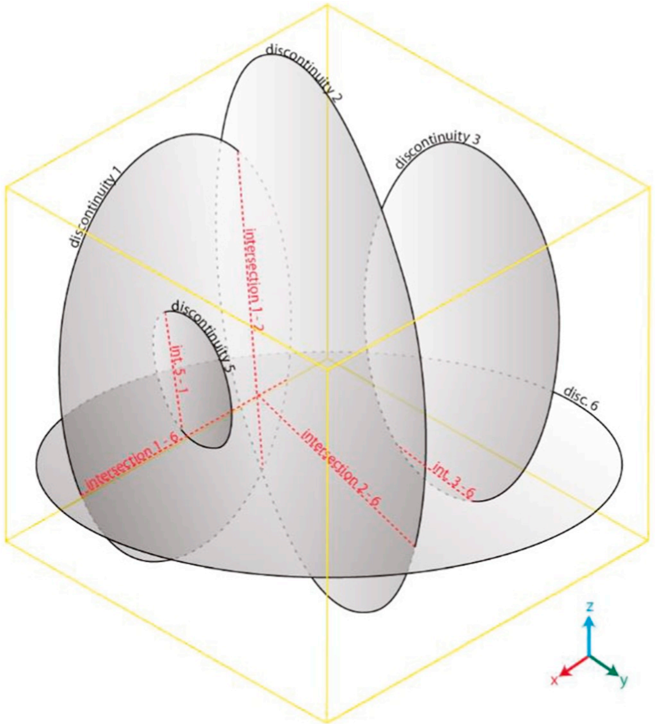

Fig. 9. Example showing lines of intersection of circular discontinuities.

3DM Analyst© has a dedicated application for the identification and mapping of discontinuities that helps the operator to map them easily. In this work, we started from the same image dataset and created a digital model using 3DM Analyst. At the end of the model generation, 32 stereo-pairs were selected to have a complete 3D representation of the studied area. The stereo-pairs provided a 3D view of the studied area that was used to detect and map the discontinuities. The obtained results are compared in Chapter 4.

3.3.2. Semi-automatic detection of discontinuities

The point cloud generated using the SfM-based photogrammetric procedure in Agisoft Photoscan was analyzed with three different open-source algorithms for the semi-automatic detection of discontinuities: i) Discontinuity Set Extractor (DSE) proposed by Riquelme et al. (2014), ii) qFacet Fast Marching and iii) qFacet Kd-tree. The second and third algorithms are plugins for CloudCompare proposed by Dewez et al. (2016).

The first method identifies and defines the algebraic equations for different planes by applying an analysis based on a coplanarity test on neighboring points, finding principal orientations by Kernel Density Estimation, and identifying clusters by the Density-Based Scan Algorithm with Noise (see Riquelme et al., 2014 for details). The other methods are based on two algorithms (qFacet Fast Marching and qFacet Kd-tree) that divide the initial point cloud into sub-cells, compute elementary planar objects, and then progressively aggregate the planar objects according to a planarity threshold into polygons. The boundaries of the polygons are adjusted around segmented points with a tension parameter, and the facet polygons can be exported as 3D polygon shape files. See Dewez et al. (2016) for details.

As a preprocessing step to improve the results of the semi-automatic detection, we removed from the point cloud all points that belong to vegetation. Two filter procedures were applied: the first is based on colour attributes of the points (RGB and HSV) and was implemented in Agisoft software, while the second was performed by masking the sectors with a lower density of points that characterize the vegetated areas (Fig. 8). It was impossible to completely remove all points corresponding to vegetation, especially in areas of dry grass and small shrubs. Thus their presence in the final point cloud may affect the correct recognition of discontinuities.

The semi-automatic detection of the discontinuities was performed on a PC characterized by a point surface density of approximately 10,386 points per m^2 (mean spacing between points approximately 10 mm). The parameter settings used in the different algorithms for the automatic detection of the discontinuities are described in Section 4.2.

3.3.3. Rock slope kinematic analysis

A stereonet-based kinematic analysis of the rock slope failure mechanisms (planar sliding, wedge sliding, flexural toppling, and direct and oblique toppling) was performed on the discontinuity systems detected by the manual and automatic analyses to highlight the possible differences and inconsistencies. The kinematic analyses assumed a friction angle of 30° and a lateral limit value (Goodman, 1980; Hudson and Harrison, 1997) of ± 20° from the dip direction of the outcrop face.

Whereas the planar sliding and flexural toppling kinematic analyses were performed using the orientation of all identified discontinuities, the wedge sliding and direct and oblique toppling kinematic analyses used the detected intersections between the identified discontinuities. The intersections were calculated considering the discontinuities as circular objects with a diameter equal to the maximum extension of the discontinuity trace and/or plane measured on the TDOM and considering its position in 3D space (Fig. 9). Due to the good exposure of the outcrop, the estimate of the maximum extension of the fractures can

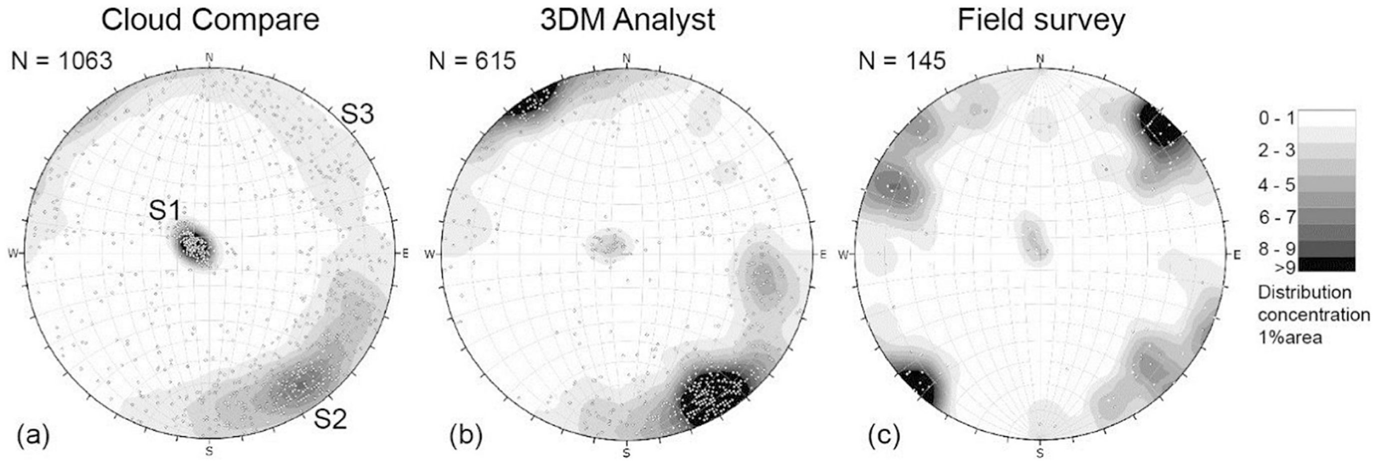

Fig. 10. Comparison of the discontinuity orientation (stereographic projections – equal angle, lower hemisphere) measured by (a) Cloud Compare, (b) 3DM Analyst software, and (c) field survey; the main discontinuity sets are indicated in (a).

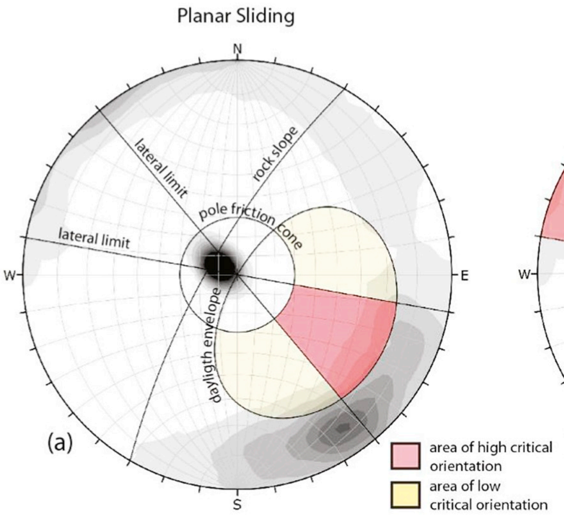

Fig. 11. Kinematic analysis of possible failure mechanisms involving individual discontinuities (a – planar sliding and b – flexural toppling). The critical pole locations fall inside the pink areas (equal angle, lower hemisphere, stereographic projections). (For interpretation of the references to colour in this figure legend, the reader is referred to the web version of this article.)

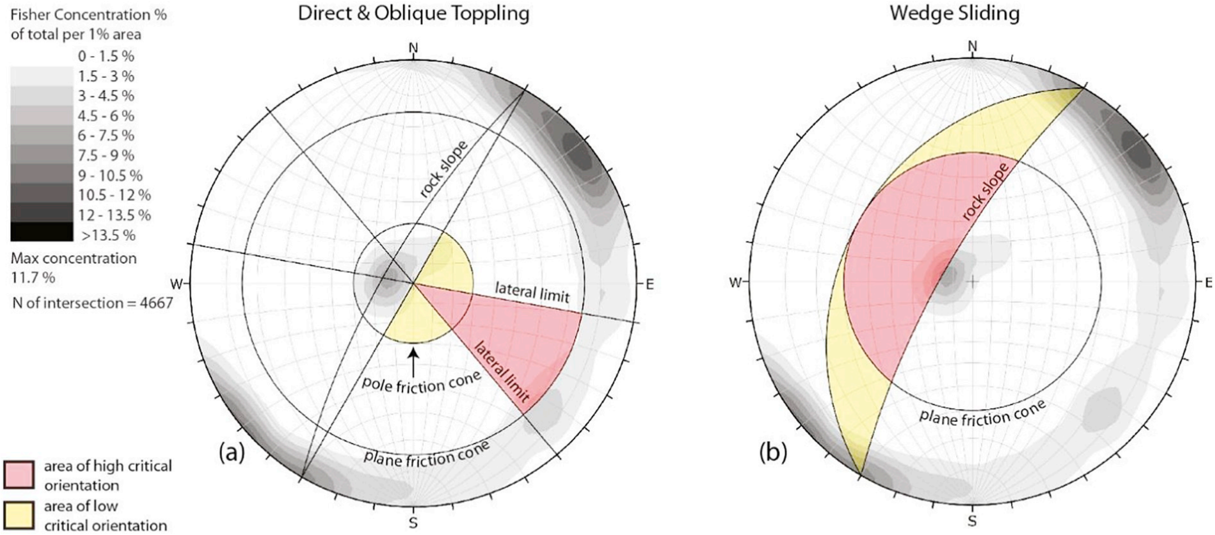

Fig. 12. Kinematic analysis of possible failure mechanisms involving intersections between discontinuities (a – direct and oblique toppling and b – wedge sliding). The critical intersection locations fall inside the pink areas. (For interpretation of the references to colour in this figure legend, the reader is referred to the web version of this article.)

Table 5
Parameters used in the DSE algorithm.

knn	h	nbins	anglevppal	cone	kσ
30	0.2	64	10	30°	1.5

be considered reliable. If two discontinuities cross each other, a discontinuity intersection is calculated and plotted on the stereonet by its trend and plunge. The kinematic analysis was first performed for an overall slope face dipping 75° towards 300°.

4. Results

The results from using the different discontinuity detection methods are presented in this section along with results from kinematic analyses of different structurally-controlled failure mechanisms. The purpose of this section is to compare and contrast the different discontinuity detection methods and their influences on the subsequent failure mode analyses.

4.1. Manual detection of discontinuities

The manual analysis of the TDOM representing the rock slope identified 1036 discontinuities using Cloud Compare. The availability of a high-resolution 3D model was very useful for the recognition of discontinuities with different orientations. In particular, the texture of the model supported the identification of discontinuities that are orthogonal to the rock wall. These discontinuities can be very difficult to detect when examining only the point-cloud.

Fig. 10 presents the measurements of the discontinuities manually obtained using Cloud Compare, those acquired by another operator that analyzed the same image dataset by 3DM Analyst© photogrammetric software, and those achieved during a field survey conducted in two accessible positions of the rock slope using a compass-clinometer.

Fig. 10 shows that all approaches recognize 3 sets of discontinuities. The dominant discontinuity set (S1) is the bedding, which is sub-horizontal. Nearly vertical, cross-cutting joints that are roughly perpendicular to the bedding are also common. These cross-cutting joints have a wide range of strikes, and they can be subdivided into different subsets (S2 and S3). The results from the three approaches are similar, and therefore for the remainder of this paper, we consider only the dataset

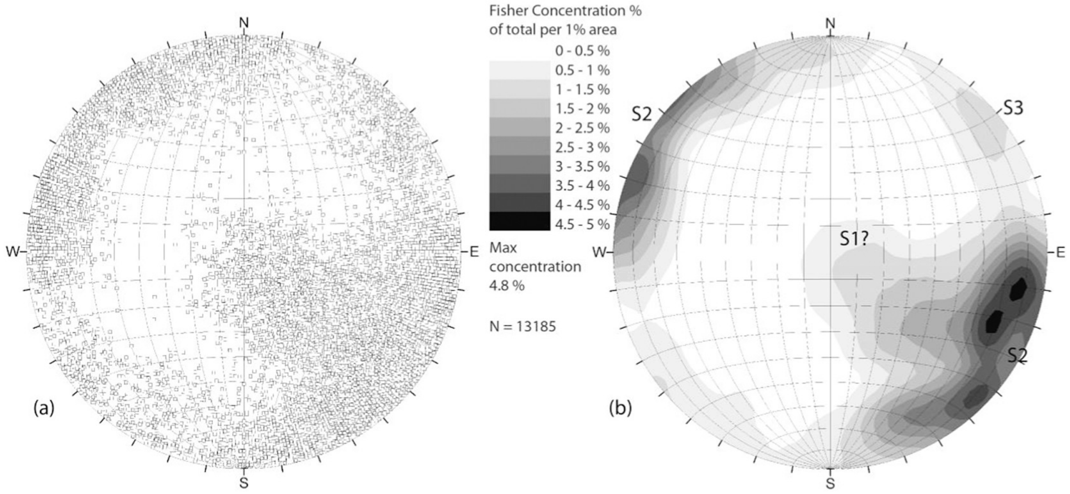

Fig. 13. Stereographic projection (lower hemisphere, equal area) of the poles to the discontinuities detected by the DSE algorithm and contour plot of pole concentrations.

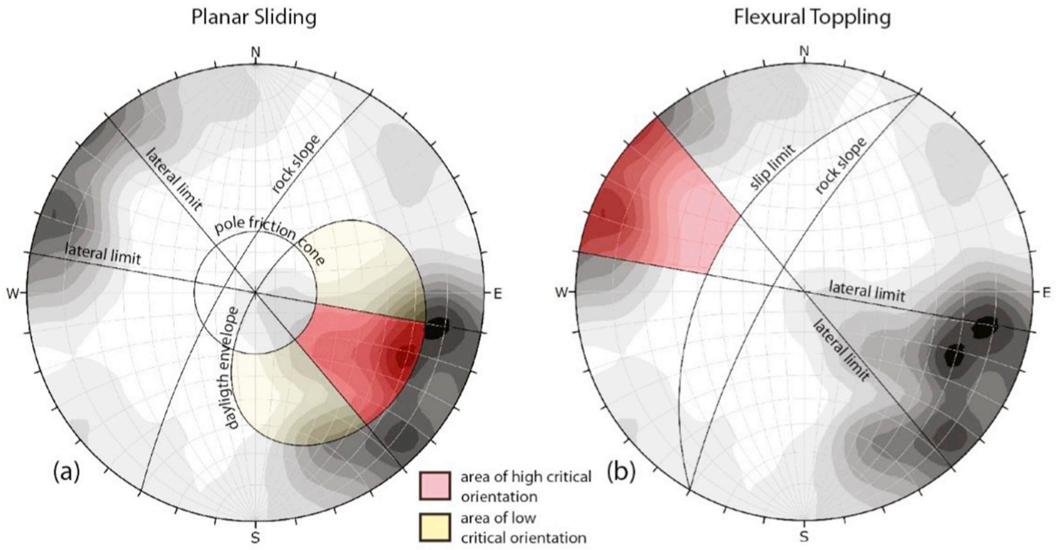

Fig. 14. Kinematic analysis of possible failure mechanisms involving individual discontinuities detected by the DSE algorithm (a – planar sliding and b – flexural toppling). The critical pole locations fall inside the pink areas (equal angle, lower hemisphere, stereographic projections). (For interpretation of the references to colour in this figure legend, the reader is referred to the web version of this article.)

(1036 measurements) obtained using CloudCompare, a freely available open-source software.

The kinematic analysis for a planar sliding mechanism indicates that 10% of the discontinuity planes (essentially formed by random discontinuities) could act as a sliding surface (Fig. 11a). The critical discontinuities for a flexural toppling failure mechanism (Fig. 11b) consist of about 4% of the total detected discontinuities and were mostly due to discontinuities in set S2.

Starting with the detected discontinuities, 4667 possible intersections were considered for the identification of possible wedge sliding and toppling (direct and oblique) instabilities. The most common failure mechanism that was identified from the kinematic analysis (Fig. 12) was wedge sliding, which involves 12% of the 4667 intersections. In particular, the most critical wedges are those formed by intersections between discontinuities in sets S2 and S3.

The kinematic analysis of the direct and oblique toppling failure mechanisms indicates that 7% of the discontinuity intersections could be critical for the block toppling mechanism (2% for direct toppling and 5% for oblique toppling).

4.2. *Semi-automatic detection of discontinuities*

4.2.1. *Discontinuity set extractor (DSE) algorithm*

The DSE algorithm (Riquelme et al., 2014) was run with Matlab© version 2.0.2 software. This method detects the structural discontinuities using a 3D point cloud by measuring the attitude of the outcrop at each point. If the point is surrounded by other coplanar points, the method statistically determines the orientation of the plane that represents these points. The parameters used to calculate the normal vector at each point, the density of the poles, and the different discontinuity sets are defined in Table 5 (see Riquelme et al., 2014 for details).

A cluster analysis was performed which considers that all points of a cluster belong to a set if they have a similar normal vector and setting the parameter $k\sigma = 1.5$ to test whether two clusters should be merged. Only clusters with > 100 points are considered as discontinuity planes.

The DSE algorithm detected 13,185 discontinuity planes in the point cloud. The orientation of the poles to these planes are plotted in Fig. 13, and they show a high dispersion with the highest pole concentration occurring in the SE quadrant of the stereonet. It is difficult to assign the

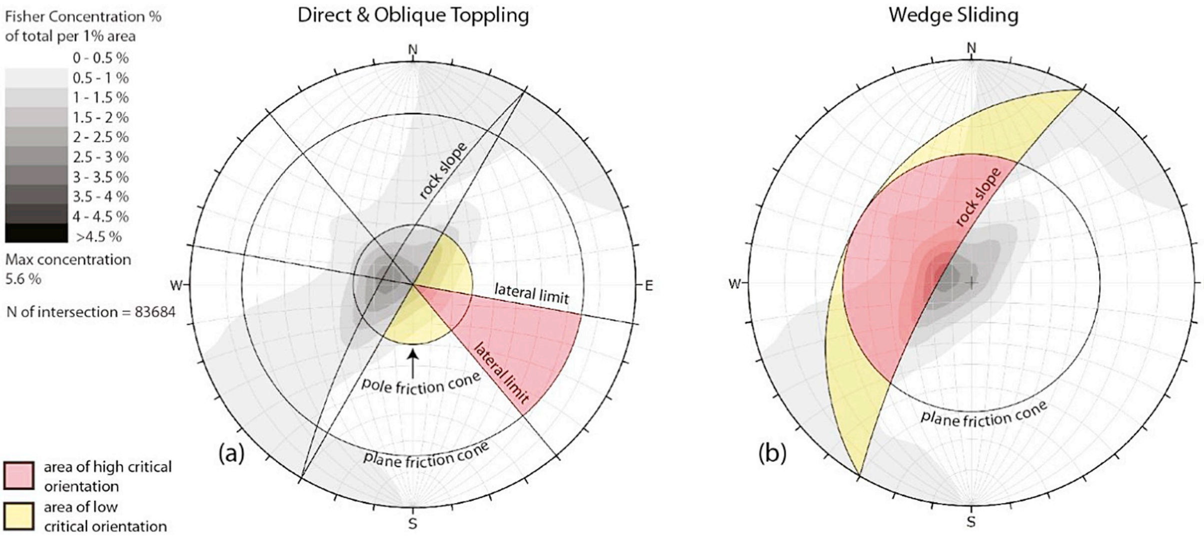

Fig. 15. Kinematic analysis of the possible failure mechanisms involving intersections between discontinuities detected by the DSE algorithm (a – direct and oblique toppling and b – wedge sliding). The critical intersections fall inside the pink areas. (For interpretation of the references to colour in this figure legend, the reader is referred to the web version of this article.)

Table 6
Parameters used in the qFacet Fast Marching algorithm.

Octree level	Max distance @ 99%	Minimum point per facet	Max edge length
8 (0.13 m)	0.1 m	100	0.86 m

detected discontinuities to individual discontinuity sets because of their dispersion. However, a comparison of these results with the manual mapping shows that the S1 set has lower visibility and blends into discontinuities from set S2. The DSE algorithm most frequently identified the steeply dipping discontinuities assigned to set S2. The S2 set has a high orientation dispersion and appears to include planes dipping at lower angles to the NW. Another minor set of discontinuities (S3) that steeply dips towards the SW was also found. These discontinuities are roughly orthogonal to Sets S2 and S1.

A kinematic analysis of possible failure mechanisms suggests that planar sliding (Fig. 14) could occur on 31% of the 13,185 discontinuities. These discontinuities typically occur in set S2 (72%). Flexural toppling (Fig. 14) involves 11% of the total number of the detected discontinuities, and these belong to set S2.

The wedge sliding failure mechanism involves 39% of the 83,684 discontinuity intersections. The critical intersections for wedge sliding involve discontinuities from sets S2 and S3. Direct and oblique toppling modes involve respectively 2% and 10% of the total number of the discontinuity intersections (Fig. 15).

4.3. qFacet Fast Marching (FM) algorithm

The qFacet FM algorithm (Dewez et al., 2016) was run using the CloudCompare v.2.9 software. The qFacet FM algorithm divides the point cloud into clusters of adjacent co-planar points using a regular lattice subdivision specified by the octree structure, measures the orientation of elementary facets and groups them into encompassing planes, and classifies parallel planes into sets.

The parameters used to calculate the cell fusion (octree level), the maximum distance of a point to a best-fitting plane, the minimum number of points per facet, and the maximum edge length used to extract the plane perimeter are defined in Table 6 (see Dewez et al., 2016 for details).

Using the parameters in Table 6, the qFacet FM algorithm detected 10,460 discontinuity planes. Similar to the DSE algorithm, the

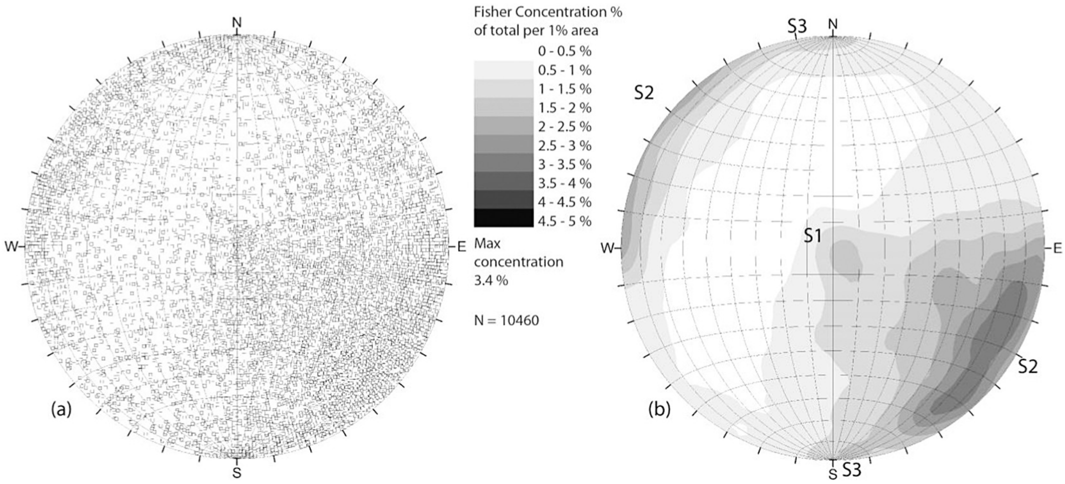

Fig. 16. Stereographic projection (lower hemisphere, equal area) of the poles of the discontinuities detected by the qFacet FM algorithm and contour plot of pole concentrations.

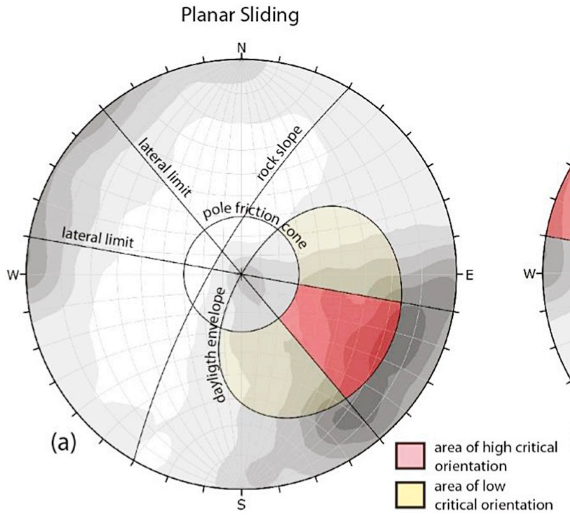

Fig. 17. Kinematic analysis of possible failure mechanisms involving individual discontinuities detected by the qFacet FM algorithm (a – planar sliding and b – flexural toppling). The critical pole locations fall inside the pink areas (equal angle, lower hemisphere, stereographic projections). (For interpretation of the references to colour in this figure legend, the reader is referred to the web version of this article.)

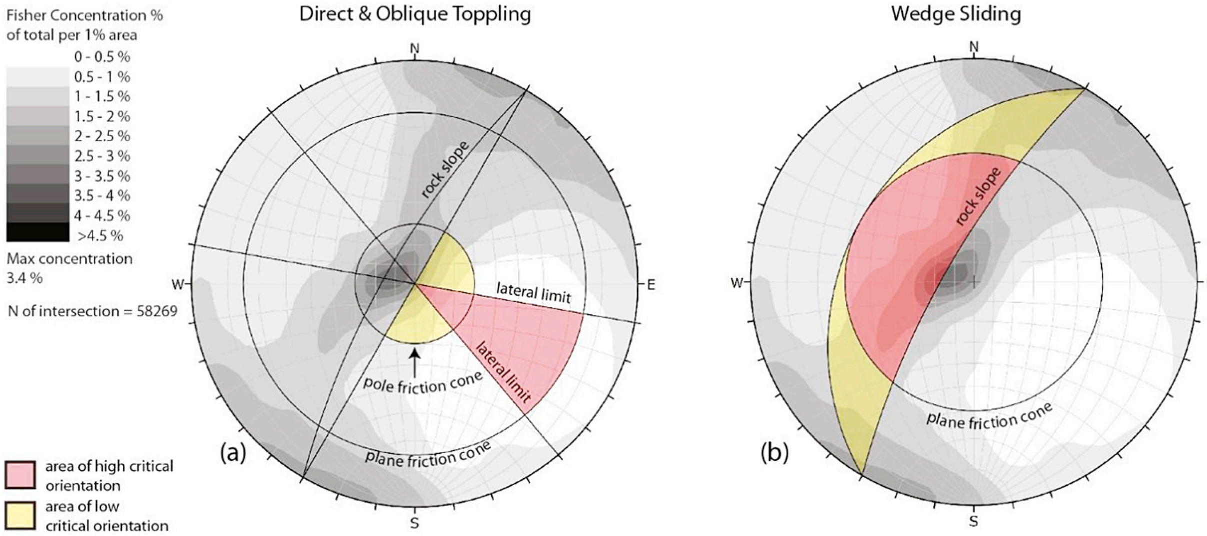

Fig. 18. Kinematic analysis of the possible failure mechanisms involving intersections between discontinuities detected by the qFacet FM algorithm (a – direct and oblique toppling and b – wedge sliding). The critical intersections fall inside the pink areas. (For interpretation of the references to colour in this figure legend, the reader is referred to the web version of this article.)

Table 7
Parameters used by the qFacet Kd-tree algorithm.

Max angle	Max relative distance	Max distance @ 99%	Minimum points per facet	Max edge length
10°	1 m	0.1 m	100	0.86 m

orientation of the poles to these planes (Fig. 16) show a high dispersion with the highest concentration occurring in the SE quadrant of the stereonet. Three principal sets of discontinuities can be recognized. The S1 set is sub-horizontal or dips slightly to the NW. The S2 set dips towards the NW with a dip angle between 50° and 90°. The S3 set is subvertical with a strike of approximately E-W.

A kinematic analysis of potential slope failure mechanisms reveals that planar and wedge sliding are potentially the most critical mechanisms (Figs. 17 and 18). Planar sliding could involve 33% of the 10,469 discontinuities, essentially those in set S2. Wedge sliding shows that 34% of the 58,269 discontinuity intersections could be critical, involving mostly discontinuities from S1 and S3. A kinematic analysis of the different toppling mechanisms indicates that these mechanisms should play a minor role in the instability of the rock slope. In particular, flexural toppling could be caused by 7% of all the detected discontinuities and direct and oblique toppling could be caused respectively by 2% and 5% of all the discontinuity intersections.

4.4. qFacet Kd-tree algorithm

The qFacet Kd-tree algorithm was run using the CloudCompare v.2.9 software. The qFacet Kd-tree is similar to the qFacet FM algorithm. Both divide the point cloud into sub-cells, then compute elementary planar facets and aggregate them progressively according to a planarity threshold into polygons. However, the Kd-tree algorithm recursively subdivides a 3D cloud into quarter cells until all points within the cell fit a best-fitting plane using the threshold defined by the root-mean-square of the maximum distance. With this technique, a lattice of elementary cells of unequal sizes is used to define the discontinuity planes.

The parameters used to calculate the cell fusion (maximum angle and maximum relative distance), the maximum distance of a point to a best-fitting plane, the minimum points per facet, and the maximum edge length used to extract the facet contour are listed in Table 7 (see Dewez et al., 2016 for details).

Using the parameters listed in Table 7, the qFacet Kd-tree algorithm

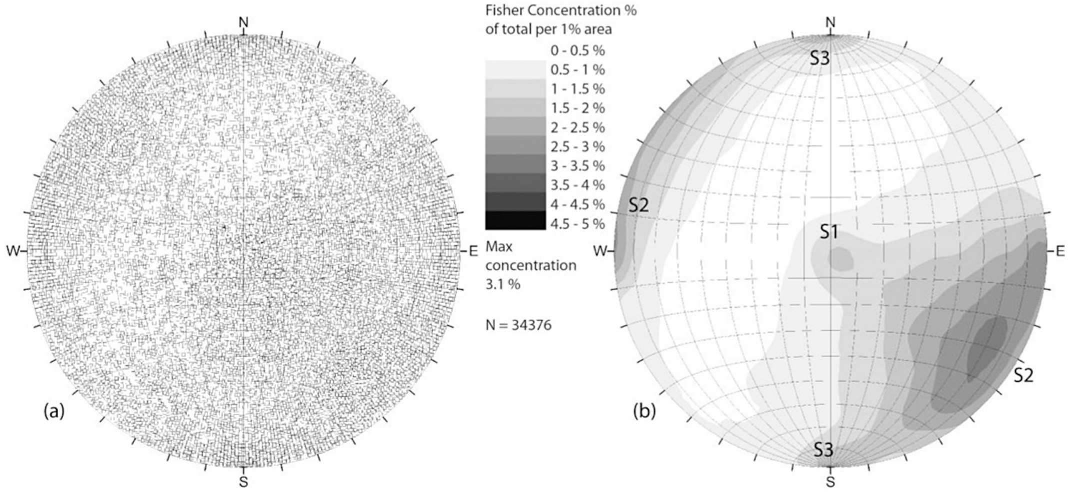

Fig. 19. Stereographic projection (lower hemisphere and equal area) of the poles of the discontinuities detected by the qFacet Kd-tree algorithm and contour plot of the pole concentration.

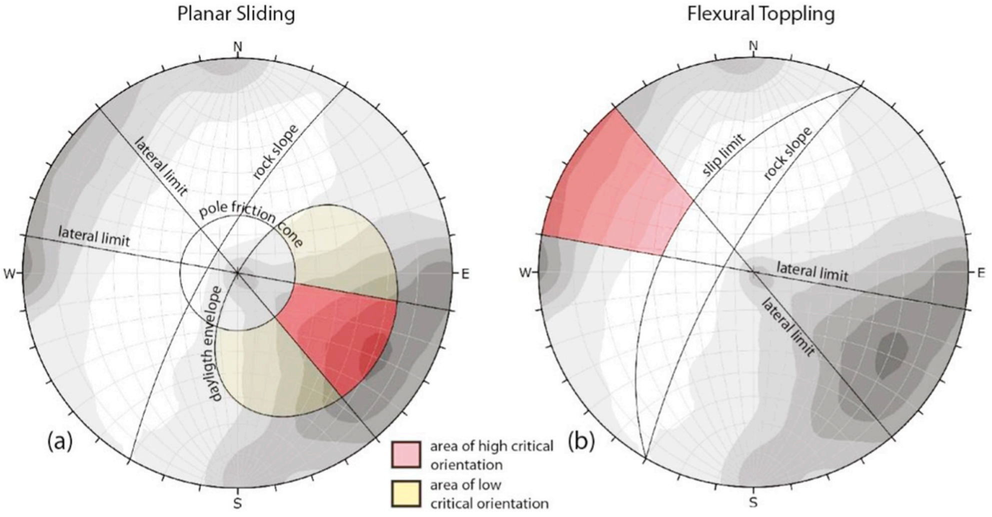

Fig. 20. Kinematic analysis of the possible failure mechanisms involving the discontinuities (a – planar sliding and b – flexural toppling) formed by the discontinuities detected by the qFacet Kd-tree algorithm. The critical pole locations fall inside the colored areas (equal angle, lower hemisphere, stereographic projections). (For interpretation of the references to colour in this figure legend, the reader is referred to the web version of this article.)

Table 8
Discontinuity length characteristics obtained with different detection methods (length in m).

	Manual detection on TDOM	DSE detection	qFacet FM detection	qFacet Kd detection
Number of discontinuities	1036	13,185	10,460	34,276
Mean length of discontinuities	5.96	2.13	1.88	1.11
Median discontinuity length	3.61	1.56	1.33	0.87
Mode of discontinuity length	1.75–2.00	1.00–1.25	0.75–1.00	0.50–0.75
Standard deviation of discontinuity length	6.37	2.13	1.62	0.80
Maximum discontinuity length	40.4	42.3	18.3	14.7
Minimum discontinuity length	0.40	0.40	0.36	0.38

detected 34,376 discontinuity planes. This is significantly more planes than was detected by the qFacet FM and DSE algorithms. Again, the planes have a high dispersion in their orientation, and the maximum pole concentration occurs in the SE quadrant of the stereonet (Fig. 19). Similar to the previous methods, three principal discontinuity sets can be recognized (Fig. 20b) with the same general orientations as identified before.

The calculated number of discontinuity intersections was > 140,000. Due to this large number, only the planar sliding and flexural toppling failure modes are considered. A kinematic analysis suggests that planar sliding could be a critical failure mechanism for 34% of the 34,376 detected discontinuities, and these discontinuities essentially occur in set S2. A kinematic analysis for flexural toppling suggests that only 8% of the detected discontinuities are critical for this mechanism.

4.5. Comparison of manual and semi-automatic detection methods

The discontinuities in the study outcrop were identified and measured by both manual and automatic analysis of the 3D model derived from a digital photogrammetric survey using a remotely piloted aircraft. A comparison between these methods is based on the overall number of identified discontinuities and the general discontinuity orientations and lengths.

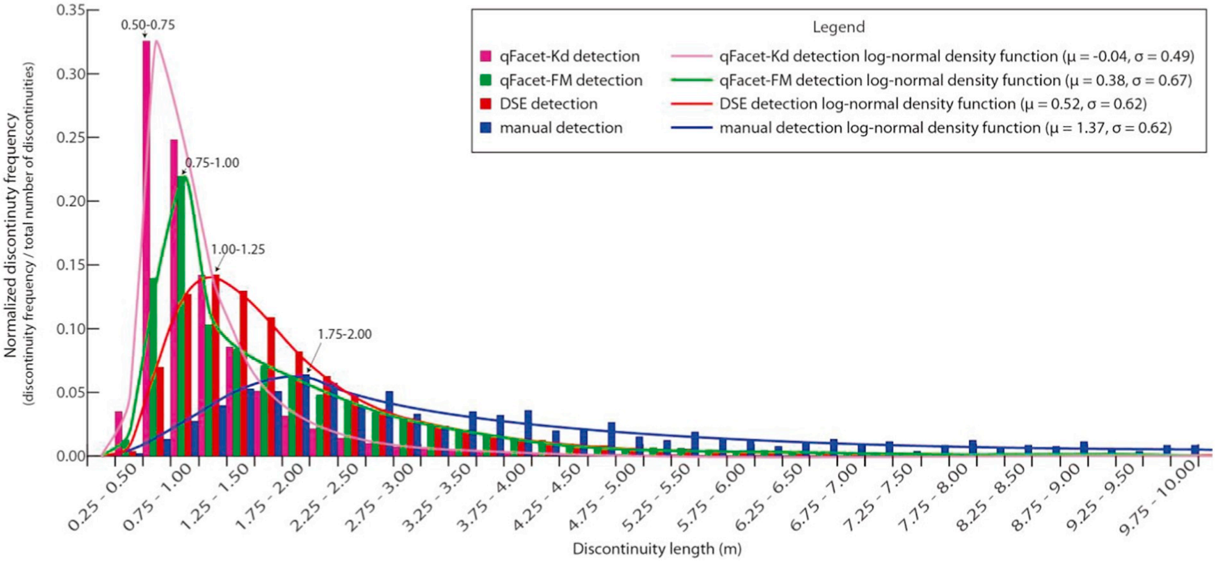

Fig. 21. Histograms of the discontinuity lengths detected by the different methods (number of bins = 100 for each histogram – solid lines show the log-normal distribution curves).

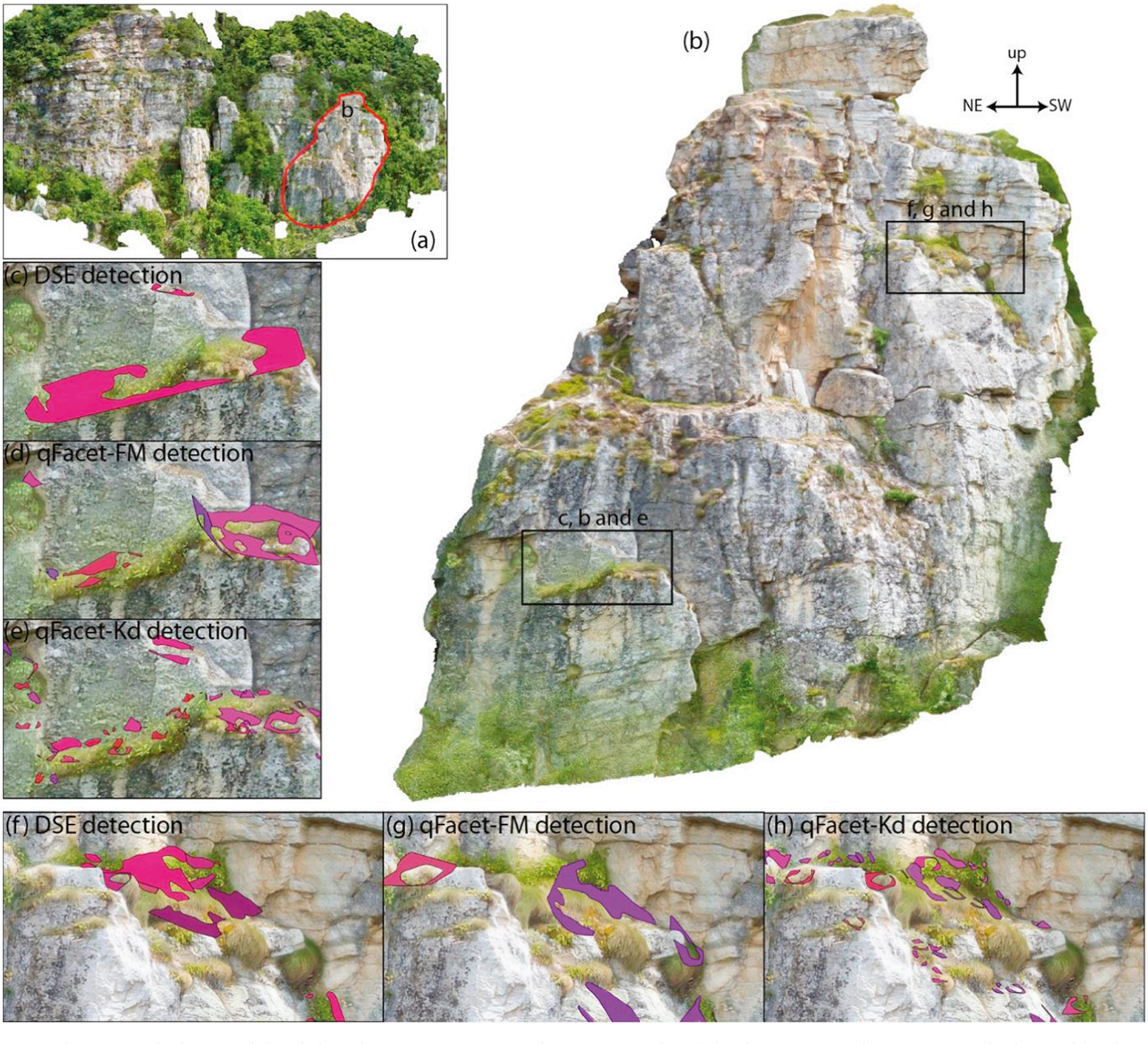

Fig. 22. Images of (a) 3D rock slope model and (b) enlargement of regions showing examples of the discontinuity planes erroneously detected by the DSE (c) (f), qFacet FM (d) (g) and qFacet Kd-tree (e) (h) algorithms due to the misinterpretation of small patches of debris and vegetation.

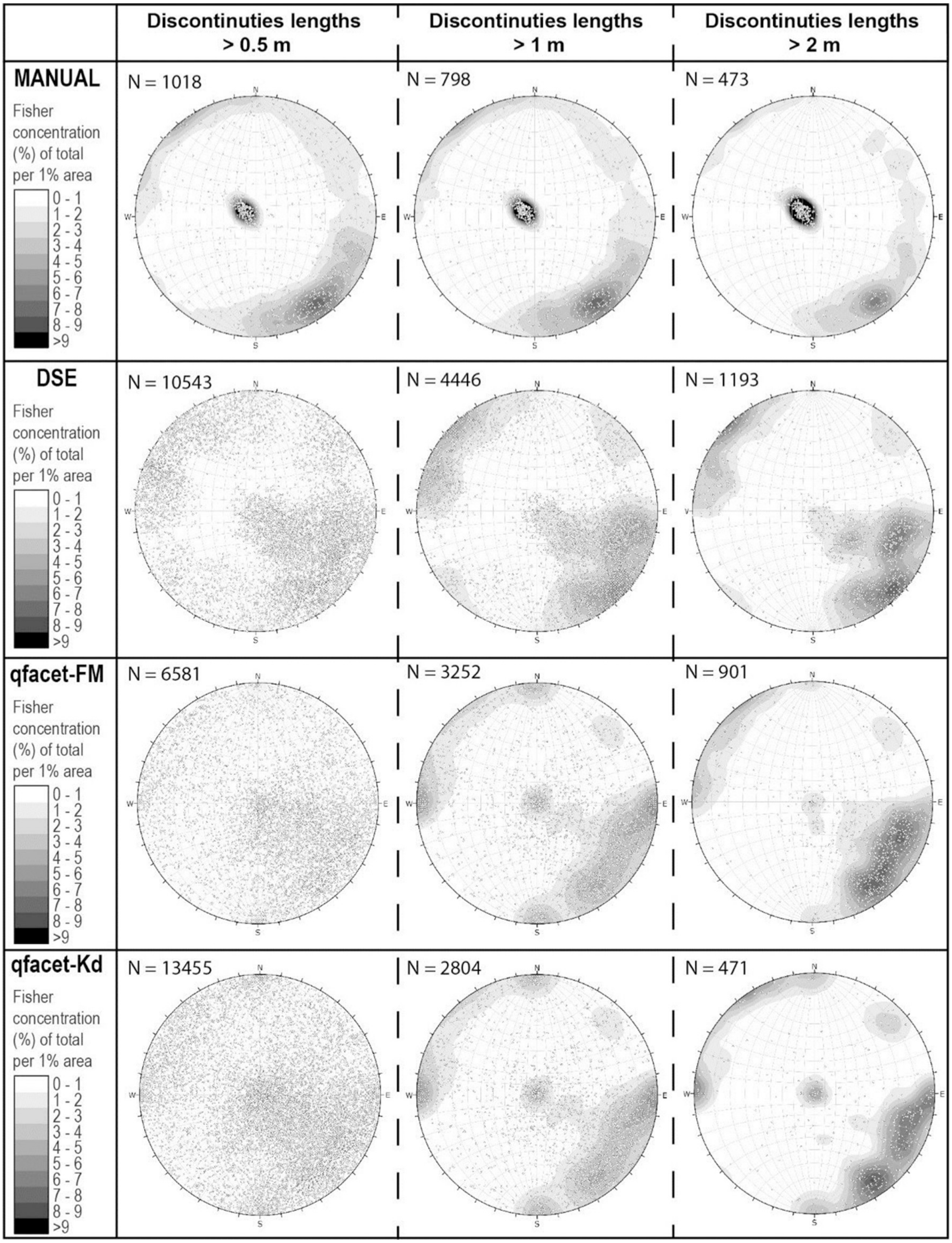

Fig. 23. Comparison of discontinuity datasets with different length cutoffs, detected by manual and semi-automatic methods. The number of discontinuities with length > 2 m are 9%, 9% and 1% of the total planes identified by DSE, FM and Kd methods, respectively.

4.5.1. *Number of identified discontinuities*

A comparison between the manually and automatically detected datasets highlights that the automatic detection methods recognize roughly 10 to 30 times more discontinuities than the manual digital mapping method (Table 8). In terms of the automatic identification methods, the qFacet Kd algorithm, as used in this study, found nearly three times more discontinuities than the other two methods. The automatic methods for discontinuity detection tend to subdivide some planes into smaller planes owing to local variations of the surface undulation and roughness, and thereby identify a larger number of presumed smaller discontinuities.

4.5.2. *Discontinuity lengths*

A summary of the discontinuity length characteristics obtained from the different methods is shown in Table 8. The length of discontinuities that were identified using the manual detection method is greater than the length of the automatically detected discontinuities. The manual detection method recognized 1036 discontinuities with a mean length

Table 9
Comparison of the kinematic analyses for different detection methods for a slope dipping 75° towards 300°.

Discontinuity detection method	Planar sliding	Flexural toppling	Wedge sliding	Direct toppling	Oblique toppling
	(% of all detected discontinuities)		(% of calculated intersections of all detected discontinuities)		
manual	10	4	12	2	5
DSE	31	11	39	2	10
qFacet FM	33	7	34	2	5
qFacet Kd	34	8	n/a	n/a	n/a

of approximately 6 m (mode ≈ 1.75), whereas the automatic methods, with the parameters used, recognized a larger number of discontinuities (> 10,459) with a smaller length (mean length < 2.14 m, mode ≈ 0.75–1.0) (Table 8; Fig. 21).

4.5.3. Discontinuity orientations

The steeper dipping discontinuities identified by manual detection were also found by the semi-automatic detection methods although there are some minor differences in the concentrations of the discontinuity dip directions. The bedding planes that are horizontal to gently dipping are arguably the most dominant discontinuity set in the rock mass. These features were easily identified during manual mapping of the TDOM. However, automatic discontinuity detection methods do not clearly recognize this set. The bedding often appears only as a trace on the nearly vertical rock faces. The automatic discontinuity detection methods can miss these features even when the bedding trace was large and was the most relevant geomechanical feature in the rock wall. The automatic detection methods can only identify planar facets, and these are often very small along the trace of the bedding and are not detected.

The automatic discontinuity detection methods return numerous planes that dip towards the NW that are not visible from the manual inspection of the 3D model. The false detection of some of these discontinuities seems to be associated with the presence of small patches of debris or grassy slopes visible along the wall (Fig. 22). The automatic detection algorithms do not properly discriminate between features that are discontinuities and those that are caused by other features captured in the 3D model.

To avoid the false detection of discontinuities due to small parts of the outcrop characterized by debris and natural slope surfaces, and taking into account the differences in the dimensions of the detected planes, we have considered only the recognized discontinuities that have a length of > 0.5, 1 and 2 m (Fig. 23). In fact, the length can be one of the more sensitive parameters conditioning the semi-automatic recognition of the fractures.

The results of this analysis (Fig. 23) indicate that as the cutoff length is increased: a) the number of the planes identified by the manual and automatic methods decreases and approaches a more similar number, b) the dispersion in the fracture orientation considerably decreases, and c) the overall discontinuity orientations resulting from the automatic detection methods used during this study (DSE, qFacet FM, and qFacet Kd) become more similar to each other and do not show any noteworthy differences.

Nevertheless, remarkable differences remain between the manual and automatic datasets: a) the numerous automatically detected planes (but not discontinuities) that dip towards the NW are still present, and b) the bedding (i.e., the most dominant discontinuity set) is still not clearly identified by the automatic methods. In any case, the choice to discriminate the detected fractures by their length appears somewhat arbitrary and may not be justifiable a priori.

4.5.4. Instability mechanisms inferred from identified discontinuities

The differences in the results from the manual and semi-automatic methods affect the interpretation of possible structurally-controlled failure mechanisms expected in the rock slope. Table 9 shows the percentage of the discontinuity planes and intersections that could be critical for each dataset, for a slope dipping 75° towards 300° and assuming a friction angle of 30°. A lateral instability limit of 20° was also used. In particular, the three datasets based on semi-automatic detection overestimate the planar and wedge sliding mechanisms by a factor of roughly 3 times compared the manual discontinuity mapping. A preliminary analysis of the collapse phenomena already affecting the slope confirms that toppling (flexural, oblique and direct) is probably the most widespread and dangerous instability mechanism, while planar and wedge sliding are less frequent. This observation was also supported by the geologists of ARPA Piemonte.

5. Conclusions

In this work, we presented a workflow for the detection of the discontinuities exposed in a sub-vertical rock slope using a remotely piloted aircraft system and digital photogrammetry (Fig. 5). This approach is particularly useful in areas where field mapping and terrestrial photogrammetry or laser scanner surveys cannot be used because the slope is inaccessible, unsafe, and characterized by a complex geometry with several shadow areas not visible from the ground. Results based on the use of CloudCompare software to measure the discontinuity orientation are presented. To evaluate the quality of the discontinuity mapping, we compared the results with in situ manual mapping and with the well-known software 3DM Analyst©.

The proposed procedure results in the generation of a 3D digital model of the rock slope; this can be referred to as a texturized digital outcrop model (TDOM). This model can be used to visually recognize and manually map discontinuities in the outcrop. In our case, a planar stereoscopic mirror device (SD2220W) that allows a stereoscopic view of the model was used. Mapping the recognized discontinuities was performed by sampling the points in the TDOM belonging to each discontinuity plane and calculating the 3D best-fit plane by a least-squares-fit approach. The discontinuity orientations were verified by comparing the manual digital mapping in the TDOM with the orientation of some control planes measured directly on the field with a

Table 10
Advantages and limitations of RPAS-DP.

Advantages	Limitations
Can accurately map discontinuities by creating a high-resolution TDOM (< 1 cm) with results comparable to field measurements	Complex vertical rock slopes could require RPAS with proximity sensors (more expensive RPAS)
Dramatic increase of data because inaccessible or hidden portions of the slope are captured in the model	Possible regulatory restrictions on RPAS flights (e.g., licenses and permits)
Substantial time savings during discontinuity orientation measurements	Wind or critical meteorological conditions can hamper image acquisition using RPAS
Repeatability of measurements by different operators at different times	Time of flight is limited by battery duration which can be critical for investigation of large areas
Safe methodology especially for an unstable rock slope	If the morphology of the study area is complex, manual remote control of RPAS can be necessary; this requires good piloting skills

compass-clinometer. The manual digital mapping generated results that are equivalent to the field measurements because the orientations were within 3° of each other.

A comparison of TDOMs generated with and without the use of GCPs shows that the difference in the relative accuracy is small. While the use of ground control points is usually the best solution, it usually takes less effort and is much faster to acquire field data only relying on the GPS coordinates recorded by the UAV. The resulting TDOM created using the digital images and their GPS coordinates may be offset from the real coordinates, but its scale and orientation should be relatively accurate.

Three different techniques to semi-automatically detect discontinuities in the DOM were tested (DSE, qFacet FM, and qFacet KD-tree). These techniques identify planes within the point cloud by finding groups of points falling within planar regions. A comparison of the results with the manual analysis shows that the semi-automatic methods tend to recognize roughly 10 to 30 times more discontinuities than the manual digital mapping method. The semi-automatic methods also tend to find smaller discontinuities, due to their tendency to subdivide the actual discontinuities into smaller planes. The automatic methods can erroneously identify planar features that do not represent real discontinuities (e.g., patches of debris or a natural slope).

The most important observation is that the automatic methods do not work well for the detection of discontinuities that are perpendicular to the slope face such as bedding planes in our case study. Geological structures that are primarily exposed on rock faces as traces, (bedding planes in the case study), are frequently the most relevant structures. The case study showed that the automatic mapping algorithms did not identify many of the bedding planes even when these occur as long trace length features in the 3D model. In contrast, the texture corresponding to these traces, which is provided in the TDOM, along with the experience of the mapper allow manual digital mapping to capture the bedding planes. The difference in detection of discontinuities can adversely influence the kinematic analysis of the rock slope failure mechanisms.

While the automatic methods have some limitations, their prime advantage is the large number of features that can be automatically mapped in a relatively short time, which could be important during an emergency operation. However, the obtained results must be accurately checked by manual validation before using them, and this can take a great deal of time.

The proposed procedure for discontinuity detection using the RPAS-DP illustrated in Fig. 5 takes into account the advantages and limitations of this technique and the algorithms for the automatic detection of discontinuities. The use of the virtual outcrop model obtained from RPAS-DP solves many practical challenges for mapping discontinuities that exist with other techniques. The advantages and limitations of the method are listed in Table 10. With a TDOM, it is possible to repeat discontinuity analysis by different operators and to use different manual and automated techniques. A high-resolution TDOM (< 1 cm) allows accurate manual analysis of a rock slope, especially if the TDOM is examined using a stereoscopic device that gives the mapper a better understanding the rock slope geometry. Nevertheless, it is important to note that field surveys are still important for validating the orientation of the TDOM and for evaluating discontinuity parameters such as aperture, roughness, and infilling.

Considering the time required to obtain the final results, we found that the automatic mapping procedures are faster than the manual method in the identification of discontinuities. However, taking into account the time needed for effective filtering of vegetation (mandatory for the automatic procedures and not so important for manual), and the validation of results, the difference in time and effort between the manual and automatic mapping becomes small. Manual mapping does depend on the experience of the operator, but the result is a sequence of selected and validated discontinuity measurements. The time that is required to complete the discontinuity mapping is important in particular if the operation is performed in an emergency condition, and the choice of manual or automatic procedure should consider the complexity of the area being mapped.

This case study discussed many critical issues when using images collected by a RPAS for the identification of rock wall discontinuities, and we hope that this paper can be a useful guide to others using a RPAS for discontinuity measurements.

Funding sources

This research did not receive any specific grant from funding agencies in the public, commercial, or not-for-profit sectors.

Acknowledgments

We thank Daniele Bormioli of ARPA Piemonte and Aldo Acquarone for their support in the identification of the Ormea case study.

References

Agisoft Photoscan Professional, 2016. Available online. http://www.agisoft.ru/.
Bellian, J.A., Kerans, C., Jennette, D.C., 2005. Digital outcrop models: applications of terrestrial scanning lidar technology in stratigraphic modeling. J. Sediment. Res. 75 (2), 166–176.
Bemis, S.P., Micklethwaite, S., Turner, D., James, M.R., Akciz, S., Thiele, S.T., Bangash, H.A., 2014. Ground-based and UAV-based photogrammetry: a multi-scale, high-resolution mapping tool for structural geology and paleoseismology. J. Struct. Geol. 69, 163–178. https://doi.org/10.1016/j.jsg.2014.10.007.
Biber, K., Khan, S.D., Seers, T.D., Sarmiento, S., Lakshmikantha, M.R., 2018. Quantitative characterization of a naturally fractured reservoir analog using a hybrid lidar-gigapixel imaging approach. Geosphere 14 (2), 710–730.
Birch, J.S., 2006. Using 3DM Analyst mine mapping suite for rock face characterization, in F. Tonon and J. Kottenstette (eds.), Laser and Photogrammetric Methods for Rock Face Characterization, Proc. 41st U.S. Rock Mechanics Symp., Golden.
Casella, E., Rovere, A., Pedroncini, A., Stark, C.P., Casella, M., Ferrari, M., Firpo, M., 2016. Drones as tools for monitoring beach topography changes in the Ligurian Sea (NW Mediterranean). Geo-Mar. Lett. 36 (2), 151–163.
Cawood, A.J., Bond, C.E., Howell, J.A., Butler, R.W., Totake, Y., 2017. LiDAR, UAV or compass-clinometer? Accuracy, coverage and the effects on structural models. J. Struct. Geol. 98, 67–82.
Chen, J., Zhu, H., Li, X., 2016. Automatic extraction of discontinuity orientation from rock mass surface 3D point cloud. Comput. Geosci. 95, 18–31.
Chesley, J.T., Leier, A.L., White, S., Torres, R., 2017. Using unmanned aerial vehicles and structure-from-motion photogrammetry to characterize sedimentary outcrops: an example from the Morrison Formation, Utah, USA. Sediment. Geol. 354, 1–8.
Colomina, I., Molina, P., 2014. Unmanned aerial systems for photogrammetry and remote sensing: a review. ISPRS J. Photogramm. Remote Sens. 92, 79–97.
Dewez, T.J., Girardeau-Montaut, D., Allanic, C., Rohmer, J., 2016. Facets: a CloudCompare plugin to extract geological planes from unstructured 3D point clouds. In: International Archives of the Photogrammetry, Remote Sensing and Spatial Information Sciences. 41.
Gigli, G., Casagli, N., 2011. Semi-automatic extraction of rock mass structural data from high resolution LIDAR point clouds. Int. J. Rock Mech. Min. Sci. 48 (2), 187–198.
Giordan, D., Hayakawa, Y., Nex, F., Remondino, F., Tarolli, P., 2017. The use of remotely piloted aircraft systems (RPAS) for natural hazards monitoring and management. Natl Hazards Earth Syst. Sci. Discuss. https://doi.org/10.5194/nhess-2017-339.
Giordan, D., Manconi, A., Tannant, D.D., Allasia, P., 2015. UAV: Low-cost remote sensing for high-resolution investigation of landslides. In: Geoscience and Remote Sensing Symp. (IGARSS). IEEE, pp. 5344–5347.
Gomes, R.K., de Oliveira, L.P., Gonzaga, L., Tognoli, F.M., Veronez, M.R., de Souza, M.K., 2016. An algorithm for automatic detection and orientation estimation of planar structures in LiDAR-scanned outcrops. Comput. Geosci. 90, 170–178.
Gonçalves, J.A., Henriques, R., 2015. UAV photogrammetry for topographic monitoring of coastal areas. ISPRS J. Photogramm. Remote Sens. 104, 101–111.
Goodman, R.E., 1980. Introduction to Rock Mechanics (Chapter 8). John Wiley, Toronto, pp. 254–287.
Guo, J., Liu, S., Zhang, P., Wu, L., Zhou, W., Yu, Y., 2017. Towards semi-automatic rock mass discontinuity orientation and set analysis from 3D point clouds. Comput. Geosci. 103, 164–172.
Hudson, J.A., Harrison, J.P., 1997. Engineering Rock Mechanics – An Introduction to the Principles. Pergamon Press.
Humair, F., Pedrazzini, A., Epard, J.L., Froese, C.R., Jaboyedoff, M., 2013. Structural characterization of turtle mountain anticline (Alberta, Canada) and impact on rock slope failure. Tectonophysics 605, 133–148. https://doi.org/10.1016/j.tecto.2013.04.029.
Jaboyedoff, M., Metzger, R., Oppikofer, T., Couture, R., Derron, M.H., Locat, J., Turmel, D., 2007. New insight techniques to analyze rock-slope relief using DEM and 3D-imaging cloud points: COLTOP-3D software. In: Rock mechanics: Meeting Society's Challenges and Demands. 1. pp. 61–68.
Jaboyedoff, M., Oppikofer, T., Abellán, A., Derron, M.H., Loye, A., Metzger, R.,

Pedrazzini, A., 2012. Use of LIDAR in landslide investigations: a review. Nat. Hazards 61 (1), 5–28.

Jordá Bordehore, L., Riquelme, A., Cano, M., Tomás, R., 2017. Comparing manual and remote sensing field discontinuity collection used in kinematic stability assessment of failed rock slopes. Int. J. Rock Mech. Min. Sci 97, 24–32.

Lucieer, A., Jong, S.M.D., Turner, D., 2013. Mapping landslide displacements using Structure from Motion (SfM) and image correlation of multi-temporal UAV photography. Prog. Phys. Geogr. 38 (1), 97–116.

Nex, F., Remondino, F., 2014. UAV for 3D mapping applications: a review. Appl. Geomatics 6 (1), 1–15.

Niethammer, U., James, M.R., Rothmund, S., Travelletti, J., Joswig, M., 2012. UAV-based remote sensing of the Super-Sauze landslide: evaluation and results. Eng. Geol. 128, 2–11.

Powers, P.S., Chiarle, M., Savage, W.Z., 1996. A digital photogrammetric method for measuring horizontal surficial movements on the Slumgullion earthflow, Hinsdale County, Colorado. Comput. Geosci. 22 (6), 651–663.

Pringle, J.K., Westerman, A.R., Clark, J.D., Drinkwater, N.J., Gardiner, A.R., 2004. 3D high-resolution digital models of outcrop analogue study sites to constrain reservoir model uncertainty: an example from Alport Castles, Derbyshire, UK. Pet. Geosci. 10 (4), 343–352.

Remondino, F., El-Hakim, S., 2006. Image-based 3D modelling: a review. Photogramm. Rec. 21 (115), 269–291.

Riquelme, A.J., Abellán, A., Tomás, R., Jaboyedoff, M., 2014. A new approach for semi-automatic rock mass joints recognition from 3D point clouds. Comput. Geosci. 68, 38–52.

Salvini, Riccardo, Mastrorocco, Giovanni, Seddaiu, Marcello, Rossi, Damiano, Vanneschi, Claudio, 2017. The use of an unmanned aerial vehicle for fracture mapping within a marble quarry (Carrara, Italy): photogrammetry and discrete fracture network modelling. Geomatics, Natural Hazards and Risk 8 (1), 34–52. 10.1080/19475705.2016.1199053.

Seers, T.D., Hodgetts, D., 2016. Extraction of three-dimensional fracture trace maps from calibrated image sequences. Geosphere 12 (4), 1323–1340.

Slob, S., Hack, R., Van Knapen, B., Kemeny, J., 2004. Automated identification and characterization of discontinuity sets in outcropping rock masses using 3D terrestrial laser scan survey techniques. In: Proc. of the ISRM Regional Symp. EUROCK Eurock, pp. 439–443.

Spreafico, M.C., Francioni, M., Cervi, F., Stead, D., Bitelli, G., Ghirotti, M., Girelli, V.A., Lucente, C.C., Tini, M.A., Borgatti, L., 2016. Back Analysis of the 2014 San Leo landslide using combined terrestrial laser scanning and 3D distinct element modelling. Rock Mech. Rock. Eng. 49 (6), 2235–2251. https://doi.org/10.1007/s00603-015-0763-5.

Sturzenegger, M., Stead, D., 2009. Close-range terrestrial digital photogrammetry and terrestrial laser scanning for discontinuity characterization on rock cuts. Eng. Geol. 106, 163–182. https://doi.org/10.1016/j.enggeo.2009.03.004.

Tannant, D.D., 2015. Review of photogrammetry-based techniques for characterization and hazard assessment of rock faces. Int. J. Geohazards Environ 1 (2), 76–87.

Tannant, D.D., Giordan, D., Morgenroth, J., 2017. Characterization and analysis of a translational rockslide on a stepped-planar slip surface. Eng. Geol. 220, 144–151.

Tavani, S., Corradetti, A., Billi, A., 2016. High precision analysis of an embryonic extensional fault-related fold using 3D orthorectified virtual outcrops: the viewpoint importance in structural geology. J. Struct. Geol. 86, 200–210. https://doi.org/10.1016/j.jsg.2016.03.009.

Török, Á., Barsi, Á., Bögöly, G., Lovas, T., Somogyi, Á., Görög, P., 2017. Slope stability and rock fall hazard assessment of volcanic tuffs using RPAS and TLS with 2D FEM slope modelling. Nat. Hazards Earth Syst. Sci. 18 (2), 583–597. https://doi.org/10.5194/nhess-18-583-2018.

Turner, D., Lucieer, A., Wallace, L., 2014. Direct georeferencing of ultrahigh-resolution UAV imagery. IEEE Trans. Geosci. Remote Sens. 52 (5), 2738–2745.

Vöge, M., Lato, M.J., Diederichs, M.S., 2013. Automated rockmass discontinuity mapping from 3-dimensional surface data. Eng. Geol. 164, 155–162.

Westoby, M.J., Brasington, J., Glasser, N.F., Hambrey, M.J., Reynolds, J.M., 2012. 'Structure-from-Motion' photogrammetry: a low-cost, effective tool for geoscience applications. Geomorphology 179, 300–314.

Xu, X., Aiken, C.L., Bhattacharya, J.P., Corbeanu, R.M., Nielsen, K.C., McMechan, G.A., Abdelsalam, M.G., 2000. Creating virtual 3-D outcrop. Lead. Edge 19 (2), 197–202.